1	
2	
3	
4	
5	
6	
7	
8 9	On the Generating Mechanisms of Daily Precipitation in the Conterminous
10	United States: Climatology, Trends, and Associated Marginal and Extreme
11	Distributions
12	
13	
14	Mohammed Alshehri <sup>1,3</sup>
15	Giuseppe Mascaro <sup>1</sup> Kenneth E. Kunkel <sup>2</sup>
16 17	Kenneui E. Kunkei
18	
19	
20	1. School of Sustainable Engineering and the Built Environment, Arizona State University
21 22	Tempe, AZ, USA
23	
24	2. North Carolina Institute for Climate Studies, North Carolina State University, Asheville,
25	NC, USA
26 27	
28	3. Albaha University, Albaha, Saudi Arabia
29	or mount only floring, mount, made
30	
31	
32 33	Revised version submitted to <i>Journal of Hydrometeorology</i> September 2024
34	September 2021
35	
36	
37 38	
39	
40	
41	
42 43	Corresponding author address: Giuseppe Mascaro, School of Sustainable Engineering and the Built Environment, Arizona State University. E-mail: gmascaro@asu.edu

# 44 ABSTRACT

45	A critical task to better quantify changes in precipitation (P) mean and extreme statistics
46	due to global warming is to gain insights into the underlying physical generating mechanisms
47	(GMs). Here, the dominant GMs associated with daily P recorded at 2861 gauges in the
48	Conterminous United States from 1980 to 2018 were identified from atmospheric reanalyses and
49	publicly available datasets. The GMs include fronts (FRT), extratropical cyclones (ETC),
50	atmospheric rivers (AR), tropical cyclones (TC), and North American Monsoon (NAM).
51	Climatologies of the GM occurrences were developed for the nonzero P (NZP) and annual P
52	maxima (APM) samples, characterizing the marginal and extreme P distributions, respectively.
53	FRT is everywhere the most frequent (45-75%) GM of NZP followed by ETC (12-33%). The
54	FRT contribution declines for APM (19-66%), which are dominated by AR (50-65%) in western
55	regions and affected by TC (10-18%) in southern and eastern regions. The GM frequencies
56	exhibit trends with the same signs over large regions, which are not statistically significant
57	except for an increase in FRT (TC) frequency in the Northeast (central region). Two-sample tests
58	showed well-defined spatial patterns with regions where (1) both the marginal and extreme P
59	distributions of the two dominant GMs likely belong to different statistical populations, and (2)
60	only the marginal or the extreme distributions could be considered statistically different. These
61	results were interpreted through $L$ -moments and parametric distributions that adequately model
62	NZP and APM frequency. This work provides useful insights to incorporate mixed populations
63	and nonstationarity in P frequency analyses.
64	
65	Keywords: Precipitation, Climate classification/regimes, North America, Probability
66	forecasts/models/distribution, Trends
67	

### 1. Introduction

68

69

70

71

72

73

74

75

76

77

78

79

80

81

82

83

84

85

86

87

88

89

90

91

92

93

94

96

97

98

Theoretical arguments (Emori & Brown, 2005; Trenberth, 1999) suggest that the frequency and intensity of precipitation (P) are expected to change in a warmer climate, potentially causing negative impacts on communities and ecosystems (e.g., Cann et al., 2013; Eekhout et al., 2018; Gershunov et al., 2018; Wilcox et al., 2017). P outputs of general circulation models (GCMs) largely confirm these arguments at global and continental scales (Dong et al., 2021; Janssen et al., 2014; Prein et al., 2017; Lee et al., 2021), but their uncertainty is still high at the fine scales targeted by impact studies, even after they have been downscaled statistically or dynamically (e.g., Lopez-Cantu et al., 2020; Underwood et al., 2020). One of the main reasons is that P processes in GCMs are largely parameterized, and their spatial resolutions are still too coarse to capture small-scale orographic effects. Despite this, it has been shown that GCMs simulate better the large-scale generating mechanisms (GMs) leading to P than the associated P intensities (e.g., Eyring et al., 2021; Zhang & Villarini, 2021), and that this capacity has improved in the latest GCM versions from the Coupled Model Intercomparison Project Phase 6 (CMIP6; Priestley et al., 2020). Therefore, a strategy to refine the quantification of future changes in P mean and extreme statistics is to gain insights into the underlying physical GMs and assess how their occurrence might change in a warming climate (Barlow et al., 2019; Zhao et al., 2017). Important progress has been made over the last decade to define the GMs of P and identify them in atmospheric reanalysis and GCM simulations. One of the earliest studies was conducted in the Conterminous United States (CONUS) by Kunkel et al. (2012), who categorized the GMs of extreme daily P into seven types: fronts associated with extratropical cyclones (FRTs), extratropical cyclones but where the extreme P occurs at some distance from the fronts (ETCs), tropical cyclones (TCs), mesoscale convective systems (MCSs), air mass convection, topographic uplift, and air mass convection associated with the North American Monsoon (NAM). In that study, a hybrid approach was used to define the GMs recorded at 935 rain gauges from 1908 to 2009 based on manual inspection of weather maps and automatic 95 algorithms applied to surface pressure and temperature reanalysis datasets for the days with extreme events. Kunkel et al. (2012) showed that, nationally, about half of extreme P events are caused by FRTs whose occurrence has been increasing in time, and that ETC is the second dominant GMs.

Several studies have subsequently performed a classification of the GMs in the United States (U.S.) focusing on specific regions. Agel et al. (2015) developed a climatology of daily overall and extreme P in the northeastern U.S. in 1979-2008 finding that >75% of the extreme events are related to ETCs throughout the year, except for September when TCs cause half of the extreme days. In the same region, Marquardt Collow et al. (2016) identified the mechanisms explaining the observed increase in extreme P in summer, while Henny et al. (2022) analyzed the role of TCs and atmospheric rivers (ARs) in the fall season. Skeeter et al. (2019) associated extreme P in the southeastern U.S. in 1950-2016 with four weather types defined according to the spatial synoptic classification scheme (Sheridan, 2002), and found an increase in the annual number of extreme P events associated with "moist tropical" days. Mullens (2021) showed that FRT is the most dominant mechanism responsible for heavy P in coastal regions of Texas for the period 2003-2018 and that drier P years were due to the lower number of ETC and summer convection events. Slinskey et al. (2020) examined the climatology of ARs across the CONUS from 1981 to 2016, finding that this GM occurs most often during fall and winter in the western regions, spring across the Great Plains, and fall in the Midwest and northeastern regions. Earlier studies analyzed the role of MCSs and the NAM on warm-season P in central (Fritsch et al., 1986) and southwestern (Adams & Comrie, 1997) U.S., respectively.

The findings of these and other studies have significantly increased our understanding of the GMs of P in the U.S. However, there are still critical open research questions. Most of the prior efforts focused on extreme P (Barlow et al., 2019), while little is known about the effects of the GMs on all nonzero P rates that are important for water resources management and ecosystems (e.g., Guan et al., 2020; Hou et al., 2014) and of which the extremes are a subsample. Moreover, it is still unclear under which conditions and at which locations different physical GMs produce P magnitudes with similar or diverse ranges and statistical properties, or, in other words, that are samples of the same or multiple statistical populations. This piece of information would allow improving P frequency estimates currently based on the hypothesis of independent and identically distributed (i.i.d.) samples (e.g., Bonnin et al, 2004; Mascaro, 2020), which are required in many practical and scientific applications.

In this paper, we addressed these research needs by gaining new insights into the climatology of the occurrence of the dominant GMs of both nonzero and extreme P over the CONUS, and into the statistical distributions of the associated P rates. For this aim, we expanded

- the classification of Kunkel et al. (2012) by (1) considering all nonzero P days at 2861 gauges of
- the Global Historical Climatology Network daily (GHCNd) located in the CONUS (NCEI 2023),
- and (2) creating a GM dataset by combining publicly available datasets for some GMs and
- applying fully automated techniques to detect other GM types using reanalyses such as the
- Modern-Era Retrospective analysis for Research and Applications, Version 2 (MERRA-2; Gelaro
- et al., 2017). We identified six GMs over the period 1980–2018 when MERRA-2 was available,
- including ETC, FRT, NAM, AR and TC, and other unclassified mechanisms (Others). Note that
- AR was not included in Kunkel et al. (2012), while other categories present in that study were
- not included for the reasons explained in Section 3a.
- The dataset of daily P records and associated GMs at the GHCNd gauges was used to
- investigate four main research questions:
- 141 (1) How do the climatological occurrences of the GMs of nonzero daily P and the corresponding
- extremes vary spatially in the CONUS? Does the spatial variability change when evaluated at
- annual and seasonal scales?
- 144 (2) What is the relative contribution of the six GMs to nonzero P and does it vary when
- 145 considering the extremes? If yes, in which geographic regions?
- 146 (3) Has the annual occurrence of each GM changed from 1980 to 2018?
- 147 (4) Are the P values produced by the different GMs characterized by different statistical
- distributions? Is this true for both all nonzero P rates and the corresponding extremes or for
- just one series type, and why?
- To answer these questions, we performed several statistical analyses involving the computation
- of climatological metrics, a new framework for trend detection in count time series at multiple
- sites, two-sample tests whose power in applications with P records has been recently quantified
- by Mascaro (2024), *L*-moment ratios (Hosking, 1990), and the fitting of parametric distributions
- that adequately model the frequency of nonzero P and the extreme values.

### 2. Study Area and Dataset

- We used daily P records from GHCNd rain gauges located in the CONUS for the period
- 157 1980-2018 (total of 39 years) when the GMs of daily P were identified (see Section 3a). We
- initially selected 3169 gauges and, for each gauge, we excluded the years with more than 10% of
- missing days; we then eliminated the gauges with less than 30 years of data. This resulted in a

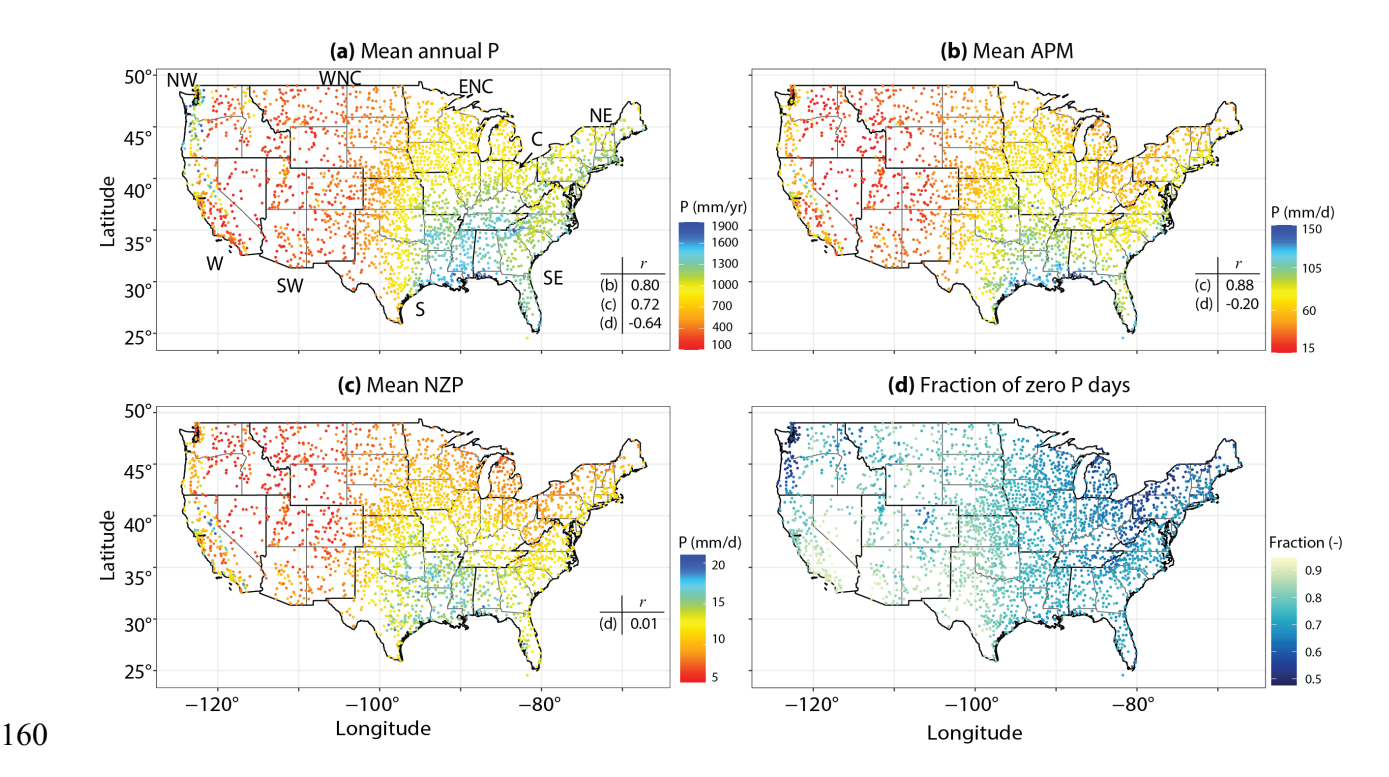


**Figure 1.** Location of the selected 2861 stations of the Global Historical Climatology Network daily (GHCNd) in the Conterminous United States (CONUS), along with the National Climatic Data Center (NCDC) climatic regions defined as East North Central (ENC; 342 gauges), West North Central (WNC; 365 gauges), Northwest (NW; 171 gauges), West (W; 195 gauges), Southwest (SW; 246 gauges), South (S; 618 gauges), Southeast (SE; 312 gauges), Central (C; 390 gauges), and Northeast (NE; 222 gauges). The gauges are color-coded based on (a) the mean annual P, (b) the mean annual P maxima (APM), (c) mean nonzero P (NZP), and (d) fraction of days with zero P in 1980-2018. The spatial correlation coefficients, *r*, between the map shown in panels (a)-(c) and the other maps (indicated with the panel letter) are also reported.

total of 2861 gauges that cover the country with good density, as shown in Fig. 1. To summarize our results, we used the nine National Climatic Data Center (NCDC) climate regions (Karl & Koss, 1984), which are also reported in Fig. 1a (see the figure caption for a definition of the regions' acronyms that will be used throughout the paper). We investigated differences between the GMs of P focusing on nonzero P (NZP) values and the annual P maxima (APM, also known as Rx1day) series, with the latter being a subsample of the former capturing the extreme P values. Depending on the analyses, the APM were extracted considering the entire NZP series or separately from the NZP produced by a given GM. Fig. 1 presents the spatial variability of mean annual P, mean APM, mean NZP, and fraction of zero P days in 1980-2018. The metrics vary widely across the country with mean annual P, APM, and NZP exhibiting lower magnitudes in

most of the western regions, where the fraction of days with zero P can exceed 0.9, and higher values in the central, eastern, and most of the southern regions, as well as in the Pacific Northwest, where the fraction of dry days can be as low as 0.5. The pattern of mean annual P exhibits a relatively high correlation with those of all other metrics (correlation coefficient, r, above |0.64|), while mean AMP and NZP exhibit the largest spatial correlation (r = 0.88).

## 3. Methods

a. Identification of the generating mechanism of daily precipitation

This study leveraged the availability of datasets developed by one of the co-authors (Kunkel) and other researchers, along with publicly available products. This leveraging provided the opportunity for a deep analysis of GMs, but it also constrained certain aspects, which will be discussed herein. The processes causing P are varied and have been categorized in multiple ways. While the GM framework of Kunkel et al. (2012) adopted a phenomenological approach based on expert judgment, other studies have taken statistical approaches. For example, Prein & Mearns (2021) identified weather types causing extreme P from a cluster analysis using as input several atmospheric state variables. Davenport & Diffenbaugh (2021) used machine learning to develop an algorithm to identify extreme P days from 500 hPa geopotential height anomalies and sea level pressure. Henny et al. (2023), in a study of the Northeast U.S., took a narrower approach and categorized extreme P days into categories of tropical cyclones, atmospheric rivers, and other. These various approaches are all useful in increasing our understanding.

In broad terms, the TC and ETC represent two major GM categories for CONUS. In the Kunkel et al. (2012) study, the ETC category was broken into two variants: (1) near the ETC center and (2) along one of the fronts. In a high-level sense, this ETC breakdown approximates the quasi-geostrophic (QG) diagnostic framework for vertical motion (Holton 1972). In the QG framework, upward motion is forced by dynamical imbalances represented diagnostically as differential positive vorticity advection (DPVA) which is concentrated around the ETC low-pressure center and by warm air advection (WAA), located along the warm front ahead of the ETC center. Thus, our ETC category approximately maps to QG DPVA forcing while the FRT category maps to QG WAA forcing, although we recognize that this is only approximate since we are not calculating QG diagnostics. A third major mechanism (after TC and ETC) for P

forcing is thermodynamic instability, which manifests as convection. This is not a completely independent category since convection can be present in all of the other GMs. For example, convection is dominant in both the TC and NAM categories and is usually present along parts of the front and near the center in the ETC system. However, both isolated convection and organized convective clusters can occur independently of the TC, ETC, FRT, and NAM GMs.

The dataset of the GMs used in this study was assembled from the following sources:

- Fronts (FRTs): The automated frontal detection algorithm of Biard and Kunkel (2019) was applied to the MERRA-2 reanalysis data to produce a front location dataset at 3-hourly resolution.
- Extratropical cyclones (ETCs): Historical ETC tracks at 6-hr resolution were generated by application of the algorithm of Wang et al. (2013) to the National Centers for Environmental Prediction (NCEP)-National Center for Atmospheric Research (NCAR) reanalysis 1 (Kalnay et al. 1996).
- Tropical cyclones (TCs): TC tracks at 3-hr resolution were obtained from the International Best Track Archive for Climate Stewardship (IBTrACS) dataset (Knapp et al., 2010).
- Atmospheric rivers (ARs): AR tracks at 6-hr resolution were obtained from the data set generated by Gershunov et al. (2017).
- The characteristics of these datasets provided the constraint on the period of analysis. The beginning year of the frontal dataset is 1980, a constraint of the MERRA-2 reanalysis. The ending year of the available FRT and AR data was 2018, setting the analysis period at 1980-2018.

The determination of GM was accomplished by calculating the distance from the rain gauge to the nearest segment of each GM type. This was done at 6-hr time steps (determined by the coarser temporal resolution of the ETC and AR datasets) within the 24-hr accumulation period. The recorded distance was the closest of the four 6-hr values. The GM labeling for each P event required that the GM was within 500 km of the observation and used a hierarchical priority scheme when more than one GM was within 500 km as follows from highest to lowest priority: TC, AR, ETC, FRT, and NAM. If no GM was within 500 km, the P event was labeled as "Other" with the following exception: for events in the southwest U.S. (Arizona, California, Colorado, Nevada, New Mexico, and Utah) occurring in June, July, August, and September, such

events were labeled as North American Monsoon (NAM). The hierarchy of GM categorization, which has implications in multiple forcing situations, was motivated as follows:

- As mentioned, the TC GM label was used as long as the track was identified in IBTrACS. Our rationale for assigning TCs as the primary GM in the extratropical transition situation is that water vapor plays a dominant role in modulating extreme P magnitude (e.g., Kunkel et al. 2020). Since TCs are always characterized by high water vapor concentration, we contend that the TC contribution is always important, while that of other nearby GMs (ETC or FRT) is less certain.
- Atmospheric rivers are embedded within ETCs, usually ahead of the cold front and often extending to the warm front. The separate categorization of ARs as distinct from and prevailing over the FRT category in the western U.S. was motivated by the importance of water vapor as the modulator of P intensity highlighted by a substantial body of research. For western U.S. stations affected by ARs, around 30% of NZP days were categorized as AR, and, of those 30%, over 97% had a front located within 500 km. About 48% of NZP days at those stations were instead categorized as FRT. Thus, overall, about 78% of NZP days had a front within 500 km, and a subset of about 40% of the total of 78% FRT days were assigned the AR category.
- In the structure of an ETC, fronts usually extend to the ETC center. This is evident in our categorization as almost all (99%) of the events categorized as ETC had a front located within 500 km. The separation of ETC and FRT categories was motivated by the QG framework.

Finally, we note that the GMs analyzed here do not include all the categories of Kunkel et al. (2012). Upslope flow and air mass convection were not separately considered here because of their minor contribution to extremes as found in Kunkel et al. (2012). MCSs also were not separately categorized because there is no available dataset covering that period and mature methods for automated detection were not available at the beginning of this study. MCSs can be categorized as internally driven or externally driven by a large-scale meteorological system such as a front (Schumacher & Rasmussen, 2020). In our work, the externally driven MCSs were essentially subsumed into the category of the driving large-scale meteorological system. Internally driven MCSs not associated with a large-scale meteorological system were not explicitly identified and were by default encompassed in the Other category. Based on the

findings of Kunkel et al. (2012), we expect that the large majority of events in the Other category during the warm season are internally-driven MCSs, particularly for APM events.

b. Analyses of the occurrence of the precipitation generating mechanisms

The first three research questions outlined in the Introduction were investigated with the following analyses. We first obtained the spatial patterns of the annual and seasonal climatology of the occurrence of each GM in the NZP and APM series. This involved computing at each gauge the long-term mean occurrence (in %) of every GM in both P series. For the annual scale, these climatological means are defined as  $p_j^{NZP}$  and  $p_j^{APM}$ , respectively, for the *j*-th GM, with j = 1, ..., 6 (note that the sum of  $p_j^{NZP}$  and  $p_j^{APM}$  across the six GMs is 100). For the seasonal scale, the climatological means are defined as  $p_{js}^{NZP}$  and  $p_{js}^{APM}$ , with s = 1 (DJF), 2 (MAM), 3 (JJA), or 4 (SON) (note that the sum of  $p_{js}^{NZP}$  and  $p_{js}^{APM}$  across the four seasons for a fixed GM is 100).

We then investigated whether statistically significant temporal trends could be identified in the number of annual occurrences of the GMs in the NZP series. Let  $\{y_t\}$  be the time series of the annual occurrences of a given GM in each year t ranging from 1 to N (= 39 years). As a first level assessment, we computed, at each gauge, the linear regression slopes between  $\{y_t\}$  and t and expressed it as mean annual percentage relative to the average number of occurrences. Next, following and expanding the work of Farris et al. (2021), we designed a statistical test to quantify the degree to which the observed  $\{y_t\}$  time series are compatible with stationary processes exhibiting similar serial correlation structures and marginal distributions. As described in detail in Appendix A, we found that these two statistical properties were well reproduced by either the negative binomial (Ristíc et al., 2012; NBINAR(1)) or the Poisson (Al-Osh & Alzaid, 1987; Brännäs, 1995; Farris et al., 2021; PoiINAR(1)) integer autoregressive models of order 1, depending on the observed time series.

For each gauge, we selected the most appropriate autoregressive model, estimated its parameters based on the observed sample, and generated 1000 synthetic stationary time series. For every synthetic and observed time series, we then applied the negative binomial regression (Colin & Pravin, 1998), which is utilized when the counts are overdispersed, i.e., they exhibit variance larger than the mean, and which includes the Poisson regression as a special case when

the counts have a mean close to the variance. The regression is performed between the conditional mean of  $\{y_t\}$ ,  $\mu_t$ , and t via the relation:

304 
$$E[y_t|t] = \mu_t = \exp(b_0 + b_1 \cdot t), \tag{1}$$

where  $b_0$  and  $b_1$  are parameters estimated by maximizing the likelihood, along with the additional parameter  $\alpha_{NB}$  that controls the overdispersion of the marginal distribution ( $\alpha_{NB} = 0$  for Poisson marginals; see Colin & Pravin (1998) for details). The degree to which the observed count time series was consistent with the stationary synthetic ones was assessed through a statistical test where the null hypothesis  $H_0$  is that the series is stationary, the test statistic is  $b_1$ , and the p-value of the observed  $b_1$  is computed using the empirical distribution of  $b_1$  estimated from the 1000 synthetic samples as the null distribution. Since this test is applied at multiple sites, we accounted for field significance by applying the false discovery rate (FDR) test of Wilks (2006) at a global significance level  $\alpha_{global} = 0.10$ , chosen to account for the presence of spatial dependence. The need and utility of the FDR test were recently discussed by Farris et al. (2021).

c. Inference on the statistical properties of daily precipitation associated with different generating mechanisms

The fourth research question outlined in the Introduction aims to assess whether different physical GMs lead to similar or diverse P distributions at each site, and if the differences affect all frequencies (i.e., non-extreme and extreme P rates). To better explain this question and its importance, it is useful to clarify the terminology and introduce some symbols. The statistical distributions of the NZP and APM series are here also referred to as the marginal and extreme distributions of daily P, respectively. Since the APM are a sub-sample of the NZP series, the APM values are most likely located in the right tail of the marginal distribution. As it will be shown later, the two most recurrent GMs make up the large majority of the NZP and APM records at most gauges. Under this condition, the cumulative distribution function (CDF) of the marginal distribution, F(x), is largely controlled by the CDFs of the NZP values produced by the two most recurrent GMs,  $F_1(x)$  and  $F_2(x)$ . Our research question aims to assess whether  $F_1(x)$  and  $F_2(x)$  could be considered statistically different, i.e., they represent different statistical populations. Similar reasoning can be made for the CDF of the extreme distribution, using the symbols G(x),  $G_1(x)$ , and  $G_2(x)$ . Such an assessment has important scientific and practical

implications since it would (1) provide insights into which GMs are responsible for more intense non-extreme and/or extreme P events and where, and (2) be useful to improve P frequency estimates that are routinely done assuming i.i.d. samples, e.g.,  $F_1(x)$  and  $F_2(x)$  (or  $G_1(x)$  and  $G_2(x)$ ) are the same.

Since the true P distributions are unknown and only samples are available, the research question was investigated by applying two-sample tests to the pairs of NZP and APM records associated with the two dominant GMs at each gauge. Broadly speaking, these tests evaluate the null hypothesis  $H_0$  that two samples belong to the same population, i.e.,  $F_1(x) = F_2(x)$  or  $G_1(x) = G_2(x)$ . Following the recommendations of Mascaro (2024), we assessed differences in location with the Wilcoxon test (Wilcoxon, 1945) and the entire distribution with the likelihoodratio (S. S. Wilks, 1938) and Kolmogorov–Smirnov (Kolmogorov–Smirnov et al., 1933) tests. A brief overview of these popular tests is given in Appendix B. Since the tests are performed at multiple locations, the FDR test at  $\alpha_{global} = 0.10$  was also applied. Because only 39 years are available, the samples used to make inferences on  $G_1(x)$  and  $G_2(x)$  were the APM extracted separately for the two dominant mechanisms.

To interpret the tests' results and compare the shape of the distributions of the two mechanisms  $(F_1(x) \text{ vs. } F_2(x) \text{ and } G_1(x) \text{ vs. } G_2(x))$ , we (1) computed the first four L-moments of the samples  $\lambda_k$  (k = 1, ..., 4; Hosking, 1990) and, from these, the ratios L-CV ( $\tau = \lambda_2/\lambda_1$ ), Lskewness ( $\tau_3 = \lambda_3/\lambda_2$ ), and L-kurtosis ( $\tau_4 = \lambda_4/\lambda_2$ ); and (2) adopted the generalized gamma (GG) and the generalized extreme value (GEV) as parametric distributions for the NZP and APM series, respectively. The CDFs of the GG and GEV are provided in Appendix C. The ability of the GG distributions to adequately capture the distribution of NZP series was shown by Mascaro et al. (2023), Papalexiou & Koutsoyiannis, (2012), and Papalexiou (2022), while ample empirical evidence demonstrated that the GEV well represents the distribution of APM series (e.g., Blanchet et al., 2016; Deidda et al., 2021; Mascaro, 2020; Papalexiou & Koutsoyiannis, 2013). Here, we confirmed the appropriateness of these two distributions for the P records associated with the underlying generating mechanisms through L-moment ratio diagrams (see Fig. S1 of the Supplemental Material and its interpretation in the caption). We then estimated the parameters of the GG and GEV following the methods of Zaghloul et al. (2020) and Hosking and Wallis (1997), respectively; both approaches rely on the L-moments. As described in Appendix B, the GG and GEV distributions were also used to apply the two-sample likelihood-ratio test.

### 4. Results

363

366

367

368

369

370

371

372

373

374

375

376

377

378

379

380

381

382

383

384

385

386

387

388

389

a. Climatology of the annual and seasonal occurrence of the precipitation generating
 mechanisms

The maps of the mean annual occurrence of each GM for the NZP  $(p_i^{NZP})$  and APM  $(p_i^{APM})$  series are displayed in Fig. 2, while the results for the nine climatic regions are summarized in Fig. 3. For both types of P series, FRT is the most frequent mechanism followed by ETC; both GMs occur throughout the country and exhibit an organized spatial variability controlled by latitude and distance from the coast. The higher frequency of ETCs at northerly latitudes is a consequence of closer proximity to the mean jet stream position, while the higher frequency of FRTs toward the south reflects the structure of ETCs in which fronts can extend considerably south of the ETC low-pressure center. AR, NAM, and TC are instead less frequent and reflect more regional mechanisms. AR occurrences are restricted to the West (NW, W, and SW) because the Gershunov et al. (2017) dataset is limited to west coast events, while NAM is observed only in the Southwest (SW and W) by definition. TC occurrence is mostly restricted to lower latitudes in the eastern parts of the country (SE, S, SW, C, NE, and ENC). For a given GM, the spatial patterns of  $p_i^{NZP}$  and  $p_i^{APM}$  are relatively similar, as quantified by the correlation coefficient between the pairs of maps  $r \ge 0.71$  (reported in the left panels of Fig. 2). However, there are also several cases where  $p_i^{NZP}$  and  $p_i^{APM}$  of the same GM differ depending on the degree to which that mechanism produces the most intense P events at a given site. This is better visualized in Fig. 3, which shows that FRT is everywhere the most recurrent GM when considering the entire marginal distribution (NZP); however, its relative contribution to the extremes (APM) decreases in all regions, while that of ETC, TC, and AR becomes larger. In particular, the contribution of ETC to APM slightly or moderately increases in all regions, AR dominates APM in NW and W, and TC is a non-negligible cause of APM in C, SE, NE, and S (in order of increasing relative importance). It is worth mentioning that the mean percentage of occurrence of the GMs controlling APM is very similar to that of the GMs affecting P rates exceeding the local 95<sup>th</sup> quantile of the NZP distribution (not shown).

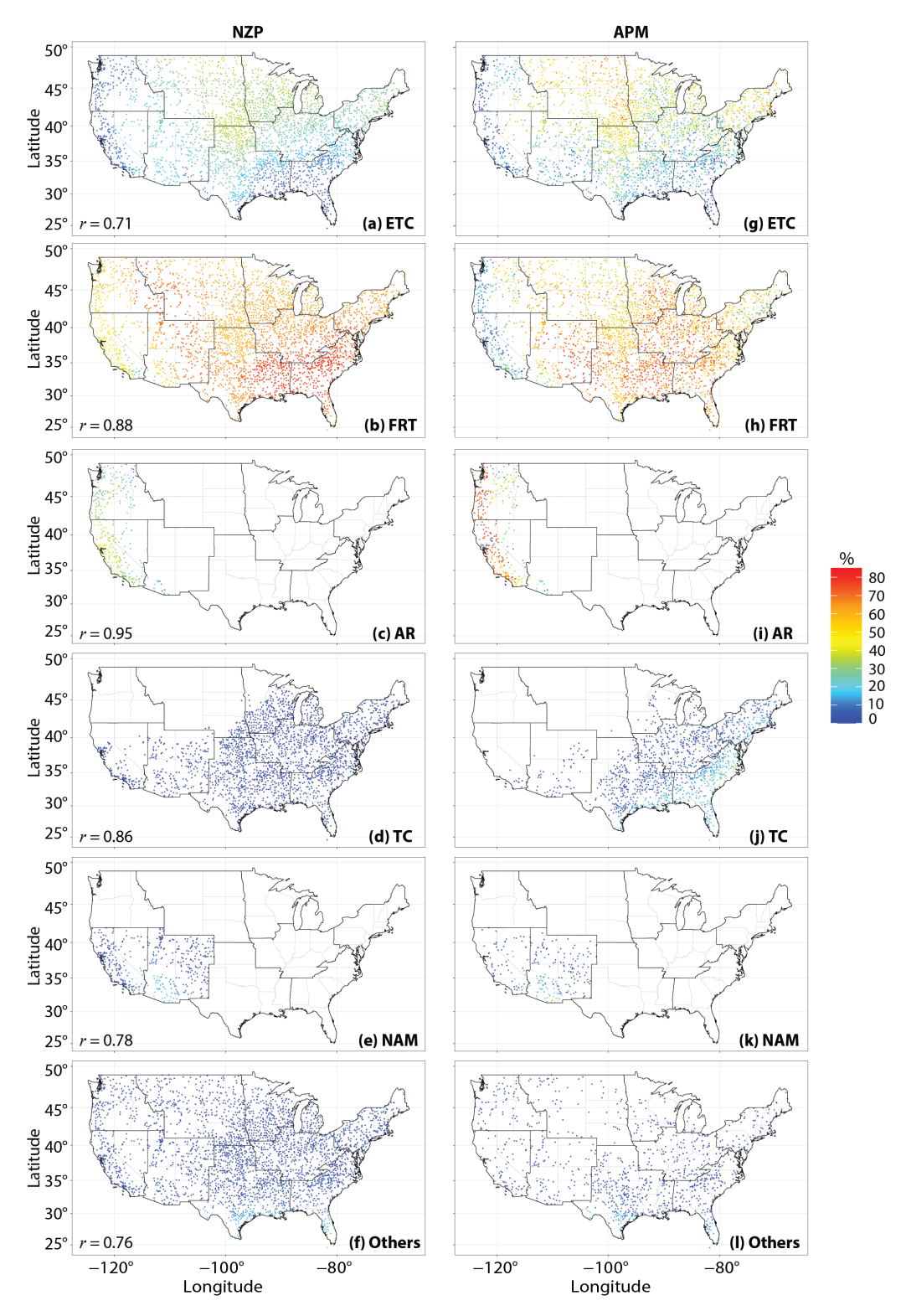


**Figure 2.** Mean annual occurrence of the P generating mechanisms of NZP,  $p_j^{NZP}$  (left panels), and APM,  $p_j^{APM}$  (right panels). The correlation coefficient between the two maps, r, is also reported in the left panels.

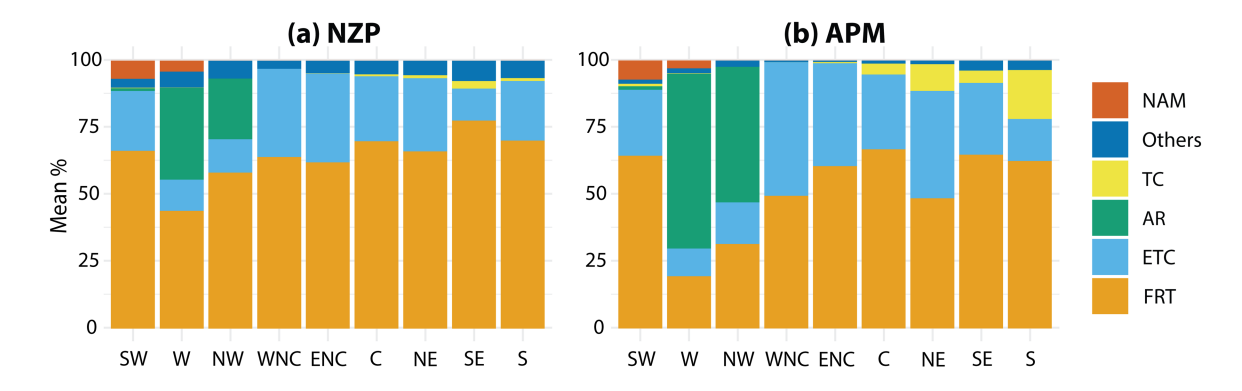


**Figure 3.** Mean annual occurrence of the six mechanisms in the nine regions for (a) NZP and (b) APM series. The percentages shown in each region are the averages of  $p_j^{NZP}$  and  $p_j^{APM}$  across the gauges of that region; since the sum of  $p_j^{NZP}$  and  $p_j^{APM}$  across the 6 GMs is 100 at each gauge, this is also true for the average across multiple gauges.

The seasonal occurrence of the GMs,  $p_{js}^{NZP}$  and  $p_{js}^{APM}$ , is visualized in Fig. 4 through bar plots for each of the climatic regions. Maps are instead shown in Figs. S2 and S3. When considering the NZP series, FRT and ETC occur in all seasons with a higher frequency in spring and summer or in winter and spring, depending on the region. The more regional GMs have a much more pronounced seasonality: AR largely occurs in winter and, to a lesser extent, in fall; TC practically only in summer and fall; and NAM, again by definition, in summer and the beginning of fall. Finally, the unclassified mechanisms (Others) are observed in all seasons but with different percentages depending on the region; as noted earlier, the majority of these in the warm season are likely to be MCSs. The seasonal occurrence of GMs of APM are generally similar to those of NZP with two important exceptions: an overall decrease in the occurrence of any mechanism in spring and an increase in summer. This indicates that, independently of the mechanism, P rates are relatively lower in spring and much higher in summer, likely due to the higher atmospheric water vapor content in the summer which is favorable for higher extreme P event magnitudes (Kunkel et al., 2020).

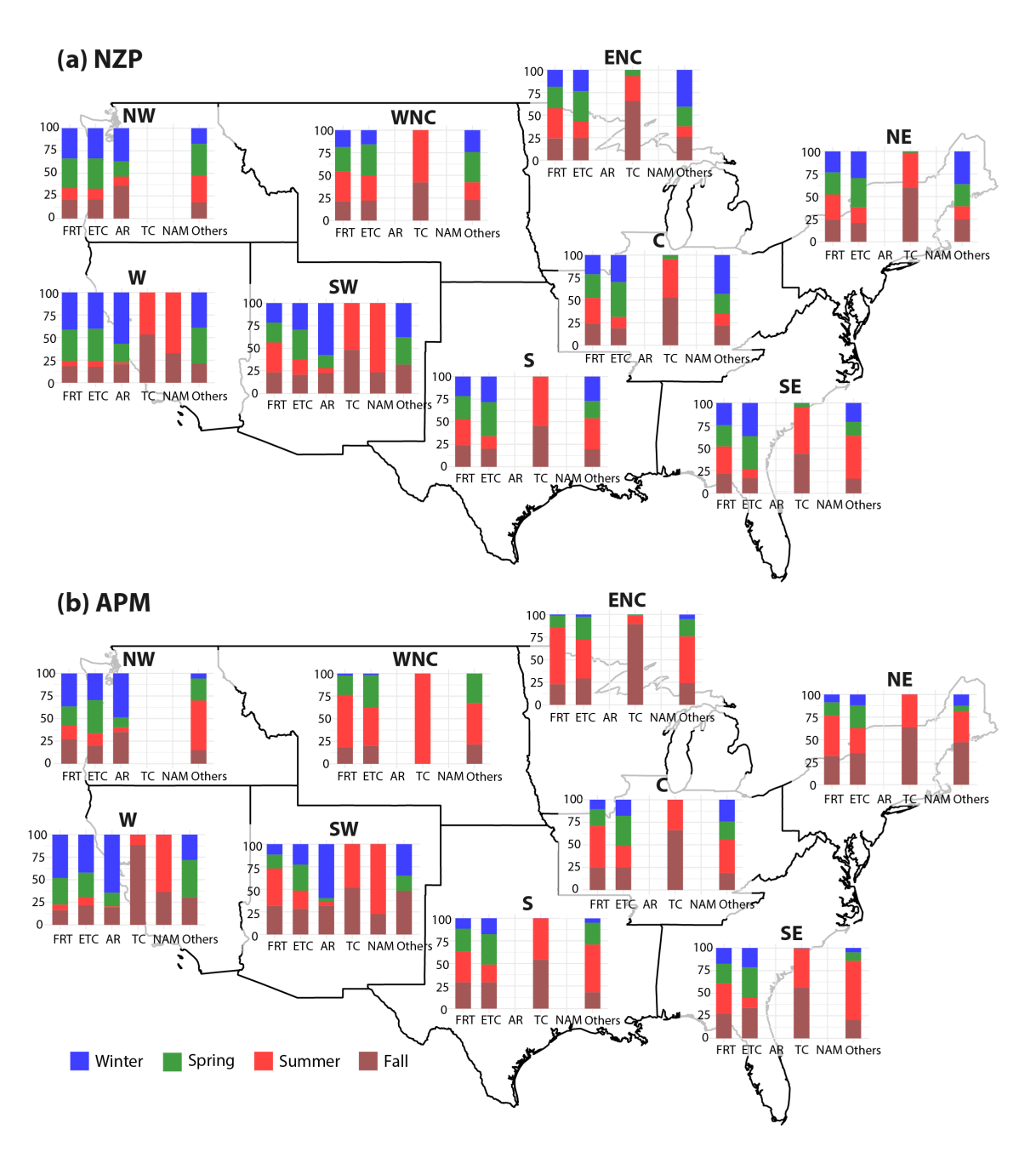


**Figure 4.** Mean seasonal occurrence of the six mechanisms across the nine regions for the (a) NZP and (b) APM series. The percentages shown in each region are the average of  $p_{js}^{NZP}$  and  $p_{js}^{APM}$  across the gauges in that region; since the sum of  $p_{js}^{NZP}$  and  $p_{js}^{APM}$  across the 4 seasons is 100 at each gauge, this is also true for the average across multiple gauges.

### b. Trends in the occurrence of the precipitation generating mechanisms

424

425

426

427

428

429

430

431

432

433

434

435

436

437

438

439

440

441

442

443

444

445

Fig. 5 displays the maps of the mean percent change in the occurrence of each mechanism in the NZP series relative to the local mean for ETC, FRT, AR, and TC. No significant changes and patterns were found for NAM, while results for Others were not considered given the possible heterogeneity of the underlying processes. The number of gauges with positive and negative trends is also provided for each region, along with the statistically significant cases based on the framework described in Section 3b. Changes over time in ETC occurrence are not statistically significant; however, distinct clusters emerge where the ETC frequency has decreased (up to -3%) in the southern and interior parts of NW, most of W, and southern SW; and increased (up to +3%) in western ENC, NE, and pockets of C, SE, and S. The pattern for FRT is instead well-defined: the frequency of this GM (1) declined in the desert regions of W, most of SW and S, and parts of SE, although these changes were largely not statistically significant; and (2) rose throughout most of the rest of the country, with several statistically significant cases in ENC and NE. The occurrence of AR diminished throughout the western regions, although the variations are not statistically significantly different from a stationary signal. In contrast, TC was observed more frequently at practically all gauges where this mechanism occurs in the southern and eastern regions, except for some sites in S. Notably, the percent increase in TCs is large (up to +8%) and statistically significant at many locations in the C region. In this region, the number of TC occurrences is relatively small, and a closer examination of the data indicated that TCs preferentially occurred in the latter part of the record in this region, leading to an upward trend.

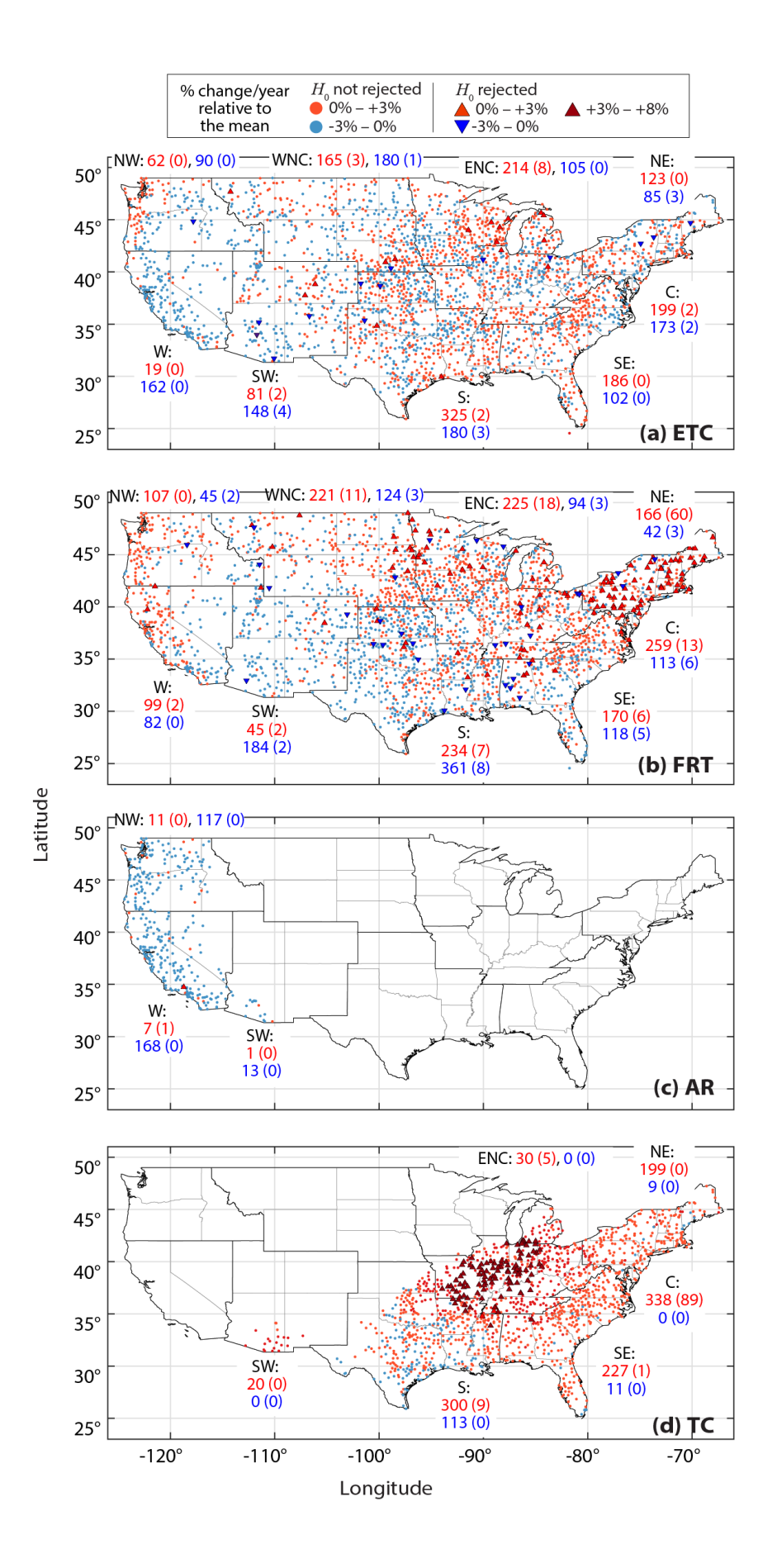


Figure 5. Mean annual percent change relative to the local mean of the occurrence of ETC, FRT,

448 AR, and TC in the NZP series. The locations where trends were found to be statistically

significant and increasing (decreasing) are shown as  $\Delta$  ( $\nabla$ ). Results are summarized for each

region based on the number of gauges with increasing (red) and decreasing (blue) trends; the

values in parentheses indicate the number of statistically significant results.

451

452

453

454

455

456

457

458

459

460

461

462

463

464

465

466

467

468

469

470

471

472

473

474

475

c. Differences between the P distributions of the two most recurrent generating mechanisms

The climatology of the annual occurrence of the GMs revealed that two GMs account for the majority of the NZP and APM records at most gauges. As mentioned in Section 3b, quantifying whether the two associated pairs of samples have different statistical properties provides insights into the relative contribution of the GMs in the marginal and extreme distributions of daily P. The spatial variability of the two most recurrent GMs for the NZP series and their combined percentage of occurrence are shown in Figs. 6a,b, respectively; bar plots are also presented in Fig. 6c to summarize the percentage of gauges in each climatic region associated with the dominant pairs of GMs. There are four pairs of dominant GMs and all include FRT as one of the GMs. FRT and ETC (hereafter, FRT&ETC) are the two most recurrent GMs across the gauges of all regions except for W and NW, where the AR category is defined and FRT&AR prevail. FRT&ETC combined represent the vast majority of all NZP observations at the gauges where this pair is prevalent (mean of 93.2%), while FRT&AR make up a slightly lower portion of the records at the associated gauges (mean of 79.1%). In the near-coastal area of the Gulf of Mexico in the S and SE regions, FRT&Others are the top two GMs comprising, on average, 90.4% of the NZP observations. Finally, in a very limited number of rain gauges in SW, FRT&NAM are the dominant GMs although they account for a lower portion of the records of these gauges (mean of 69.1%). If the focus is placed on the top two GMs of APM, more combinations of such pairs are found, but the great majority is similar to those found for NZP, except for the case of FRT&TC replacing FRT&Others in the S and SE regions (Fig. S4). Therefore, in the following, we considered the two dominant GMs of NZP to investigate differences between the associated pairs of samples of the marginal (NZP) and corresponding extreme (APM) distributions.

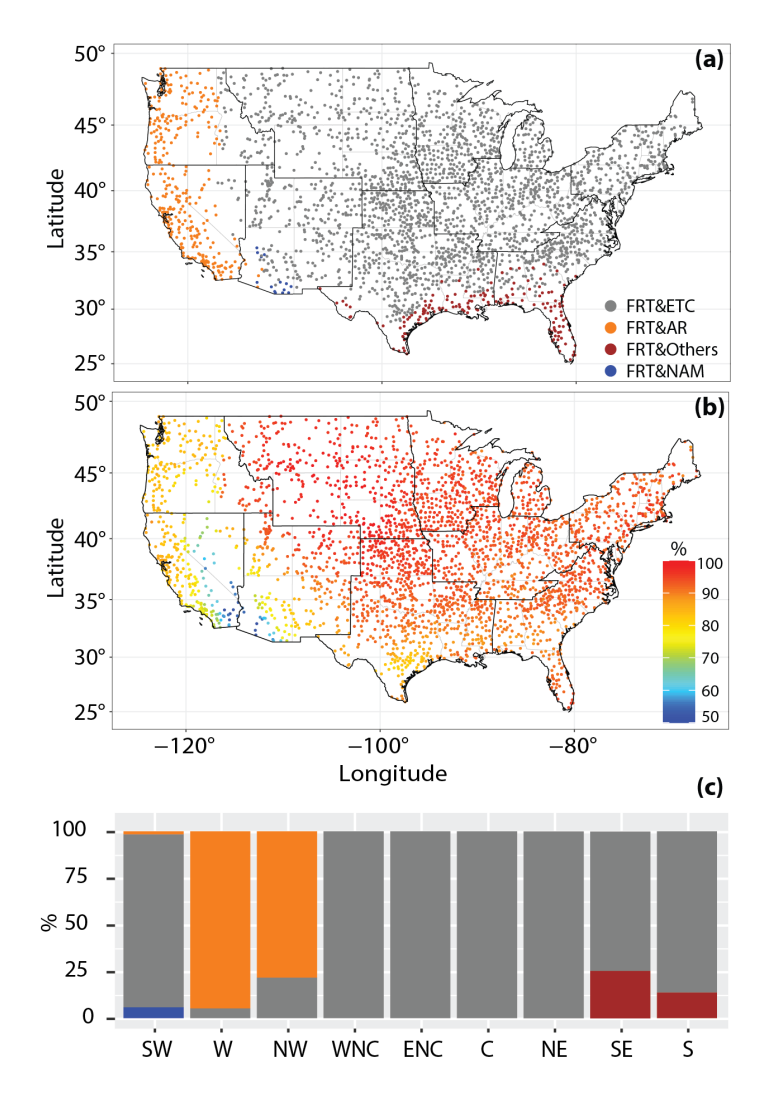


**Figure 6.** (a) Map of the two most frequent GMs of NZP. (b) Map of the percentage of combined occurrence of the two dominant GMs in the NZP samples. (c) Percentage of the gauges experiencing a given pair of dominant GMs in each climatic region relative to the total number of gauges in the region (the legend of the color is the same as panel a). All acronyms are defined in the main text.

The three types of two-sample tests were applied separately to the two pairs of NZP and APM samples associated with the dominant GMs at each gauge, providing very similar and robust results. Fig. 7 shows the outcomes for the likelihood-ratio test, while those for Wilcoxon and Kolmogorov-Smirnov tests are displayed in Figs. S5 and S6. When considering all gauges and their dominant GMs, the null hypothesis  $H_0$  of similar distributions was rejected in ~80% of the cases for the NZP series and ~60% for the corresponding APM series. This indicates that different physical GMs produce daily P accumulations characterized by clearly diverse statistical

properties when considering all nonzero values, but that these differences are less evident when focusing on the extremes. This might be due to the smaller size of the APM samples that reduces the test power (Mascaro, 2024) and/or to the similarity between the right tails of the NZP distributions of the two GMs that likely include the APM records.



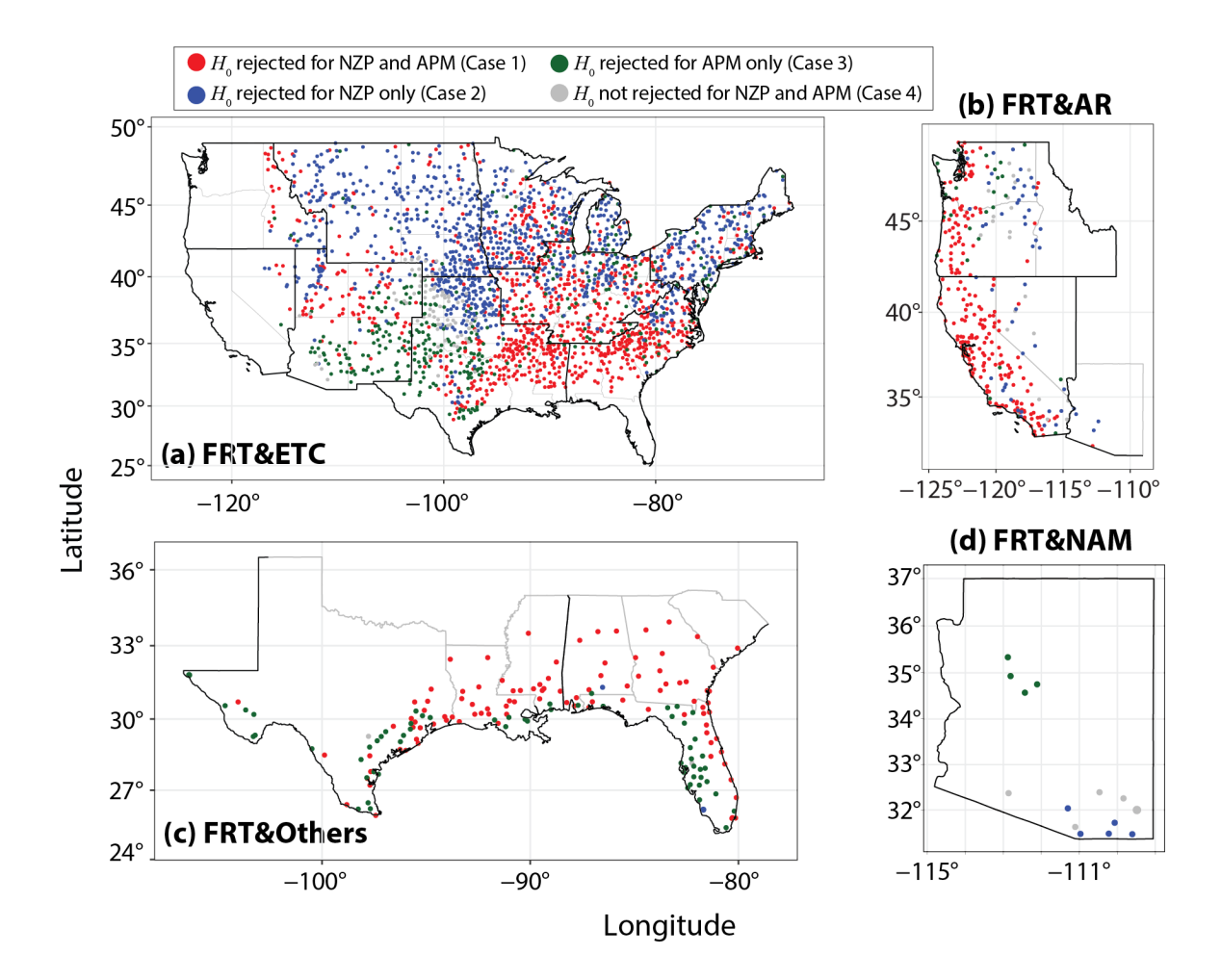


**Figure 7.** Results of the likelihood-ratio two-sample test applied to NZP and APM series associated with (a) FRT&ETC, (b) FRT&AR, (c) FRT& Others, and (d) FRT&NAM. After computing the test p-value at each site, the FDR test of Wilks (2006) was applied at a global significance level  $\alpha_{global} = 0.10$  to assess the local rejection of the null hypothesis  $H_0$ .

A closer look at the test outcomes allows better exploration of the latter point. There are three sets of gauges where different GMs result in diverse statistical distributions of daily P when considering: both all NZP values and the subsamples of the extremes (red dots; Case 1:  $H_0$  rejected for both NZP and APM); only all NZP values, but not the extremes (blue dots; Case 2:  $H_0$  rejected only for NZP); and only the extremes, but not the larger samples of all NZP rates

(green dots; Case 3:  $H_0$  rejected only for APM). Finally, in a very limited number of gauges (~5%), the two-sample test did not indicate statistically significant differences between the samples of both distribution types (gray dots; Case 4). The percentage of the four cases for each dominant pair of GMs is given in Table 1, along with the main regions where the cases occur which are well-defined in space as shown in Fig. 7. It is worth reminding that these conclusions are based on the statistical evidence associated with the significance level adopted for the tests (see Section 3c).

regions

	Case 1  H <sub>0</sub> rejected for	Case 2  H <sub>0</sub> rejected for	Case 3  H <sub>0</sub> rejected for	Case 4  H <sub>0</sub> not rejected	
	NZP and APM	NZP only	APM only	for NZP and APM	
Physical	The two NZP	The two NZP	The two APM	The two NZP	
meaning	samples come from	samples come from	samples come from	samples come	
	different	different	different	from the same	
	populations, and	populations, while	populations, while	population, and	
	so do the two APM	the two APM	the two NZP	so do the two	
	samples	samples from the same population	samples from the same population	APM samples	
	FRT&ETC				
% gauges	38%	42.7%	15.5%	3.8%	
0 0	East of S; SE; C;	WNC; north of S;	Southeast of SW;	Northwest of S;	
Main	south of ENC;	ENC; NE; north of	west of S; sparse	south of SW	
regions	north of SW	SE	locations in ENC,		
_			C, SE, and NE		
		FRT&	AR		
% gauges	68.9%	15.7%	8.6%	6.8%	
Main	NW and W	Interior regions of	NW	Center of NW	
regions		NW and W		and south of W	
		FRT&C	<b>Ath</b> ove		
% gauges	61.2%	1.2%	36.4%	1.2%	
70 gauges	East and north of S	West of SE	Along the Gulf of	West of SE	
Main	and SE	WEST OF SE	Mexico coastal	West of SE	
regions	and SE		shoreline		
	Shorenine				
	FRT&NAM				
% gauges	0%	35.7%	28.6%	35.7%	
Main		South of Arizona in	North of Arizona in	South of	

SW

SW

Arizona in SW

**Table 1.** Outcomes of the likelihood-ratio test applied to the NZP and APM samples of the two dominant GMs. For each pair of mechanisms, the percentage of gauges found in the four cases of  $H_0$  rejections or non-rejections are reported along with the main climatic regions where the cases occur.

518

519

520

521

522

523

524

525

526

527

528

529

530

531

532

533

534

535

536

537

538

539

540

541

542

543

544

514

515

516

517

To gain further insights into the reasons for these outcomes and the relations between the marginal and extreme distributions of P associated with the two dominant GMs, we displayed in Fig. 8 the scatterplots between the L-moment ratios of the NZP and APM samples for each pair of dominant GMs for Case 1 (FRT&NAM are not shown because of the very small number of gauges). The points below the 1:1 lines indicate P samples generated by FRT with larger mean  $(\lambda_1)$ , spread  $(\tau)$ , skewness  $(\tau_3)$ , and kurtosis  $(\tau_4)$  than those produced by the other dominant GM. This figure is complemented by Fig. 9 showing the empirical CDFs and survival functions of the NZP and APM series for some representative gauges along with the fitted GG and GEV distributions, respectively. FRT leads to daily P that, when considering all NZP values, have lower mean than ETC but higher variability and rates that might be much larger than the mean (i.e., lower  $\lambda_1$  and larger  $\tau$ ,  $\tau_3$ , and  $\tau_4$ ; Fig. 8a). However, the behavior is opposite when considering the subsamples of the APM, with FRT producing P extremes with higher mean and slightly lower spread than ETC, and similar skewness and kurtosis (Fig. 8b). In other words, the P rates caused by FRT are lower than those originated by ETC during more frequent events and much larger for rarer events. This is well visualized by the change in the relative position of the CDFs of NZP and APM in Figs. 9a,b. Focusing on FRT&AR, AR generates NZP values with significantly larger mean than FRT so that, despite the lower variability, skewness, and kurtosis, the P accumulations are higher across all frequencies. As a result, the APM samples for AR have also a greater mean than FRT, while the higher-order moments for the two GMs are very similar. This is shown by the very distinct CDFs for AR and FRT in Fig. 9c. Since AR events are also almost always located near a FRT, this behavior illustrates the effect of the higher water vapor transport in AR events compared to FRT (non-AR) events. Finally, for the gauges where FRT&Others prevail, FRTs cause larger P rates for events of any frequency because of the slightly (much) higher mean of its NZP (APM) samples. The close but distinct CDFs of NZP and the well-separated CDFs of APM for the two mechanisms in the example of Fig. 9d well illustrate this point.

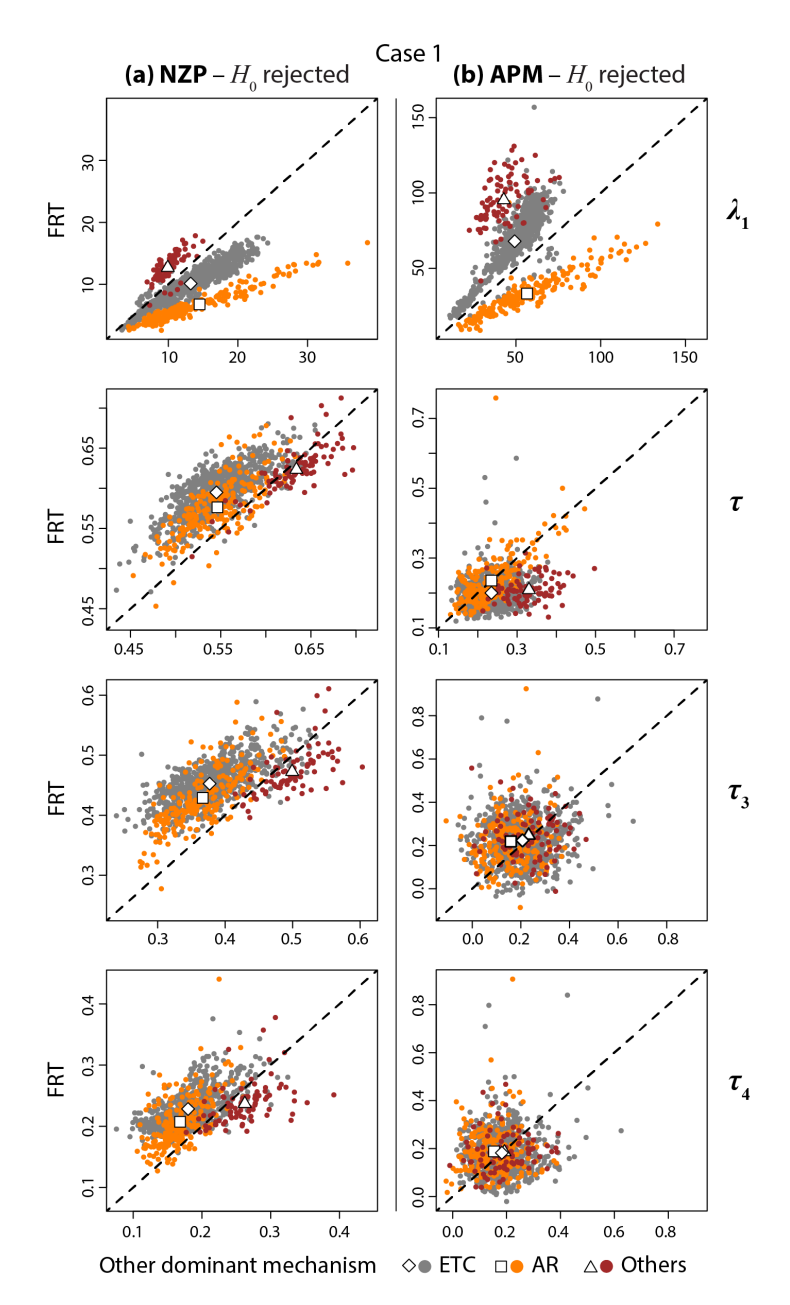


**Figure 8.** Scatterplots between the L-moment ratios of FRT vs. the second dominant mechanism (ETC, AR, Others) for the (a) NZP and (b) APM series in Case 1 where  $H_0$  was rejected for both NZP and APM samples. The means of the empirical samples are also shown with white markers.

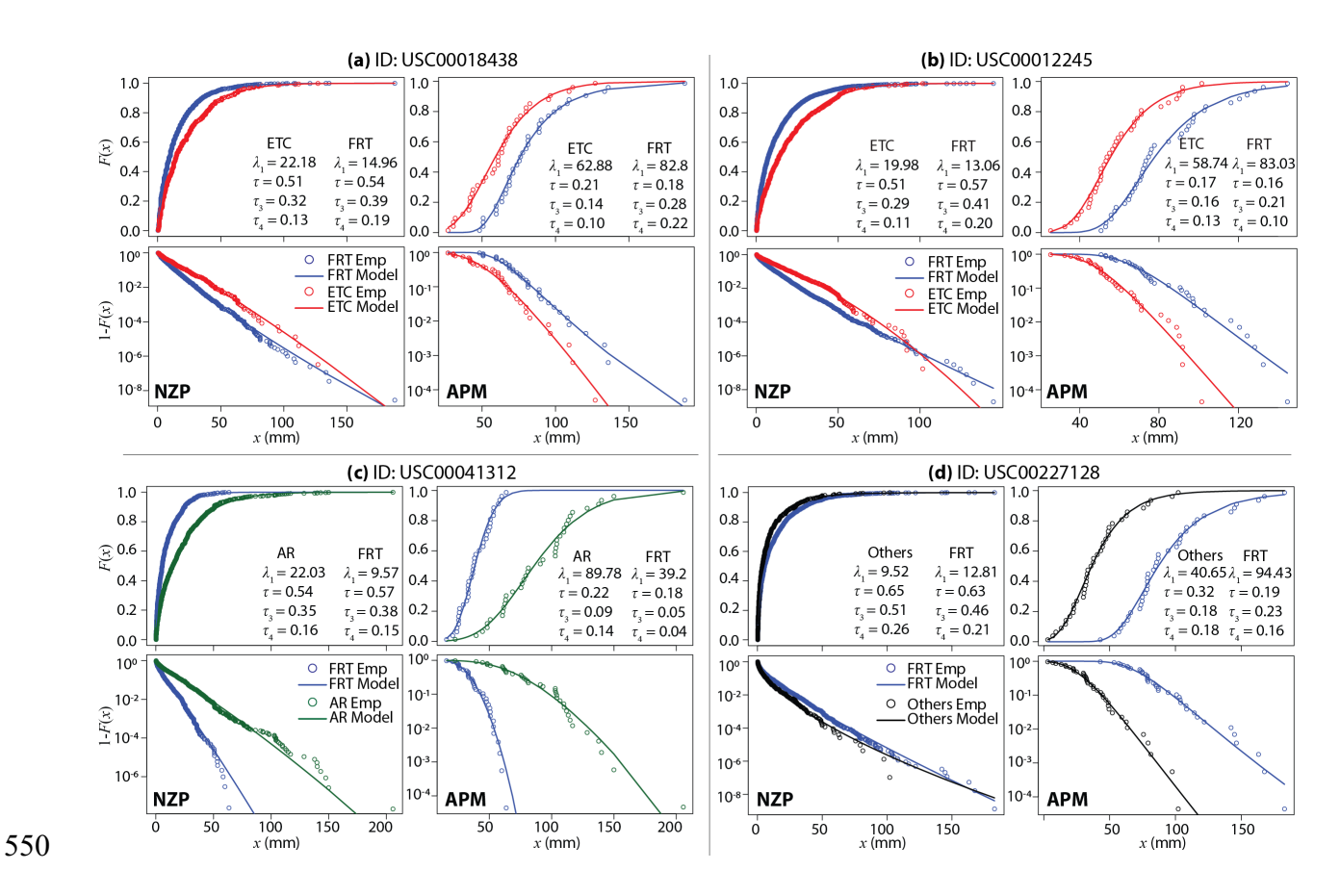


**Figure 9.** Examples of empirical CDFs and survival functions (shown to better visualize the right tails) and fitted GG and GEV distributions ("Model" in the legend) at four gauges where  $H_0$  was rejected for both NZP and APM series (Case 1) for (a)-(b) FRT&ETC, (c) FRT&AR, and (d) FRT&Others. In each panel, the CDF for NZP (APM) is shown on the top left (top right), and the survival function at the bottom left (bottom right). The values of the empirical L-moment ratios are also reported.

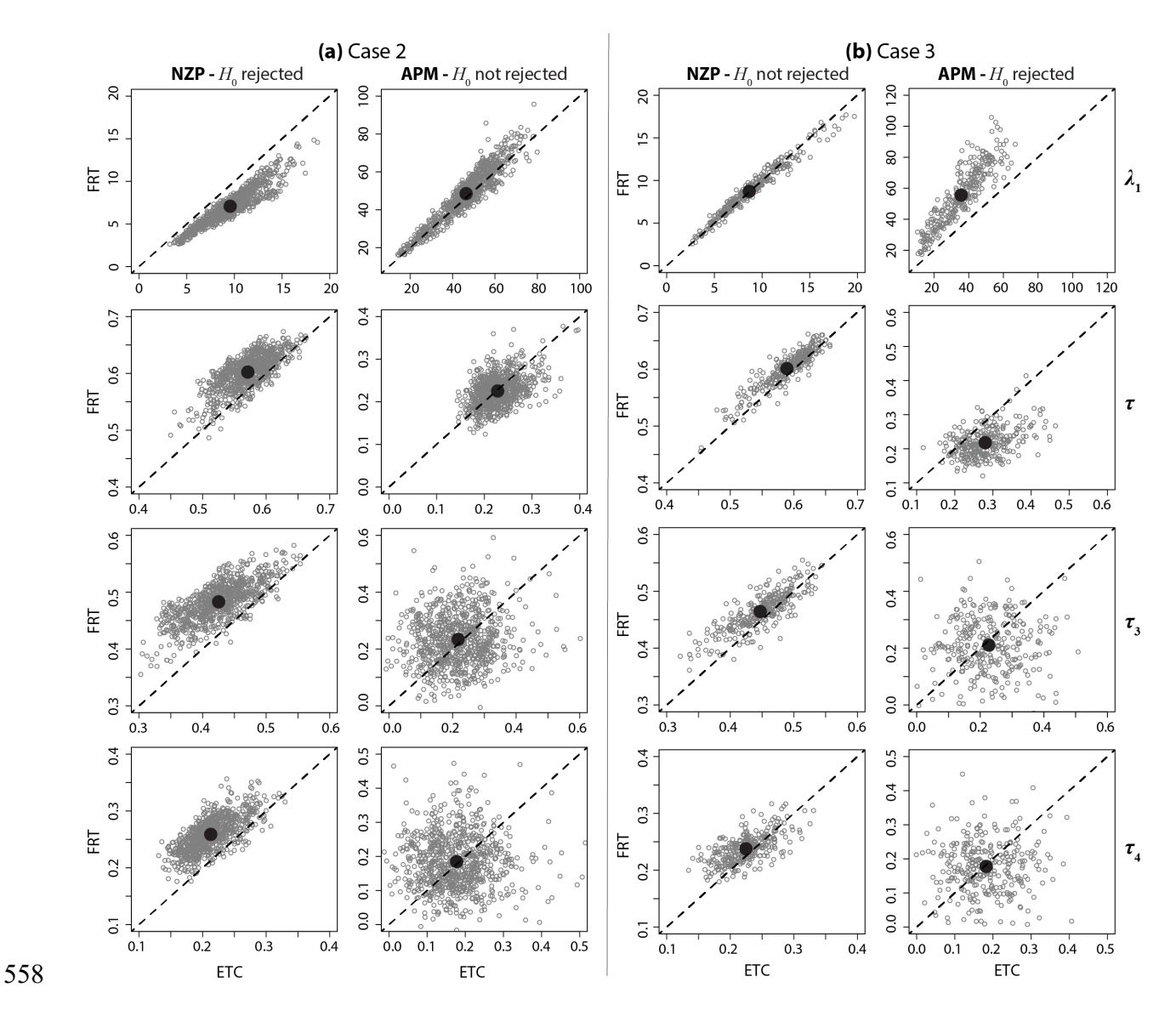


**Figure 10.** Scatterplots between the *L*-moment ratios of FRT vs. ETC for the NZP and APM series where  $H_0$  was (a) rejected for NZP but not for APM (Case 2), and (b) rejected for APM but not for NZP (Case 3). The means of the empirical samples are also shown with a black circle.

The same analyses were performed for Case 2 ( $H_0$  rejected only for NZP) and Case 3 ( $H_0$  rejected only for APM). The scatterplots of the L-moment ratios for the FRT&ETC mechanisms, covering the large majority of these cases, are displayed in Fig. 10, while examples of CDFs are reported in Fig. 11. As for Case 1, all NZP values generated by ETC have higher mean and lower spread, skewness, and kurtosis than FRT (Fig. 10a) so that the corresponding CDFs are visibly separated as shown in the examples of Figs. 11a,b. However, in these gauges mainly located in WNC, ENC, C, and NE, both GMs produce P rates within very similar ranges for the less frequent NZP events; since these extreme P values are mainly the APM, their CDFs overlap (see

Figs. 11a,b), the L-moments are similar, and  $H_0$  of the two-sample test cannot be rejected. For the Case 3 sites located in SW and S, FRT produces NZP values with a similar mean to those of ETC but slightly larger higher L-moments (Fig. 10b). Such small differences are not detected by the two-sample test so that  $H_0$  cannot be rejected. However, these differences are an indication that the right tail of the NZP distributions for FRT is heavier than that of ETC, i.e., FRT causes more intense extremes than ETC. As such, the APM samples are clearly distinguishable and  $H_0$  is rejected. This is well visualized in the examples of Figs. 11c,d, where the CDFs of the NZP for the two mechanisms largely overlap except for the right tail, while the CDFs of APM are well distinct. While a definitive analysis of the causes for this behavior is beyond the limits of this study, the QG framework suggests that FRT extremes are usually driven by WAA. Due to the thermodynamic instability often present in the warm air mass, P along the front is often enhanced by embedded convection, increasing P rates.

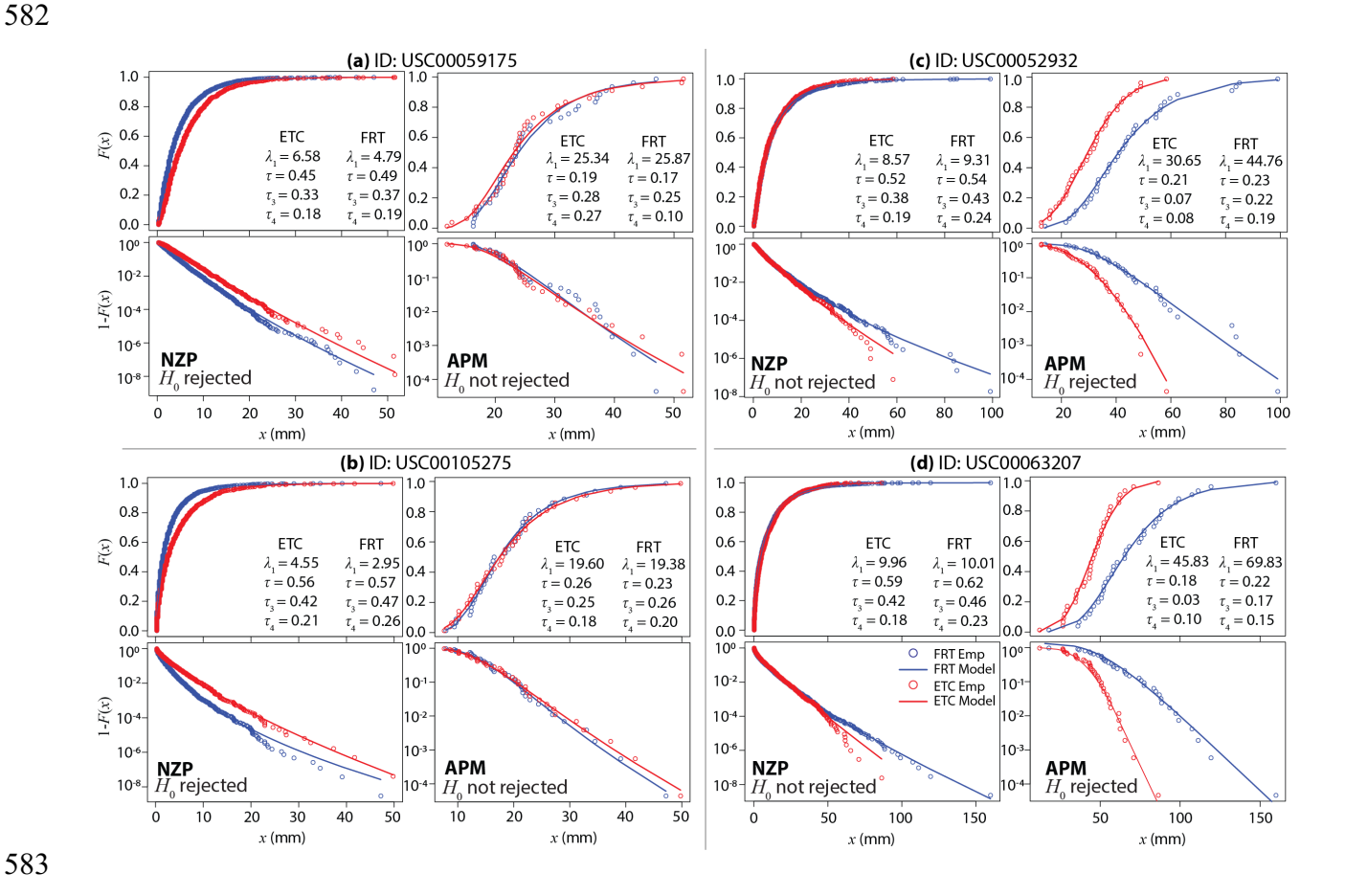


**Figure 11.** Same as Figure 9 but for gauges where  $H_0$  was (a)-(b) rejected for NZP but not for APM (Case 2), and (c)-(d) rejected for APM but not for NZP (Case 3).

# 5. Summary and Discussion

586

587

588

589

590

591

592

593

594

595

596

597

598

599

600

601

602

603

604

605

606

607

608

609

610

611

612

613614

615

a. Comparison with existing studies and new contributions to the literature

Most of the prior work focused on the GMs of extreme P, which was defined in several different ways (Barlow et al., 2019). Here, we used the APM to characterize extreme P and found that these events are largely generated by FRT and ETC in all of CONUS except for the western regions where the AR category is defined, and that these two GMs are observed in all seasons but less frequently in winter. The occurrences of FRT and ETC are largely in line with the estimates reported in the literature. In a global study, Catto & Pfahl (2013) found that the occurrence of fronts linked to extreme P in North America exhibits a longitudinal gradient ranging from >70% in the eastern part to <50% in the western side. This gradient is well visible in the map of the GMs of APM shown in Fig. 2h, although the frequencies for the eastern regions are slightly lower (see also Fig. 3b). In the NE region, the combined percentage of FRT and ETC causing APM was determined to be >75% (see Fig. 3) as in Agel et al. (2015), who considered a single category for extratropical cyclones. Our estimate of the total occurrence of FRT and ETC is also qualitatively consistent with the frequency of extreme P due to non-tropical causes reported by Moore et al. (2015) for the SE region. The AR category of our classification is defined over the W and NW CONUS and is a dominant GM of extreme P in these regions, occurring largely in winter and fall with frequencies well aligned with the study by Slinskey et al. (2020). TCs account for a non-negligible fraction of APM in S, SE, NE, and C and are observed in summer and fall, consistent with the results of Agel et al. (2015), Marquardt Collow et al. (2016), Moore et al. (2015), and Skeeter et al. (2019). Finally, NAM causes a relatively small fraction of daily APM in SW during the summer, confirming the findings of Kunkel et al. (2012) for the 1-in-5-yr P events.

As highlighted in the review of Barlow et al. (2019), a theme that has been relatively overlooked in the literature is the analysis of the GMs of non-extreme events. Here, we contributed to addressing this research gap by identifying the GMs of all daily NZP rates. We determined that FRT is the major GM of daily P events in the CONUS, accounting for 50%-75% of NZP (Fig. 3) and occurring with comparable frequencies in the four seasons (Fig. 4). The second most dominant GM of NZP is ETC, except in the W and NW regions which fall within the domain of Gershunov et al. (2017) AR dataset; there, AR is the second most dominant GM.

These western AR events are observed largely in winter, while the NZP events associated with ETC in the remainder of the country occur in all seasons with a frequency peak in winter and spring. The relative contribution of TCs to all NZP events is much smaller than their impact on the APM, while NAM contributes equally to all non-zero and extreme P in W and SW. Finally, the proportion of other unclassified GMs (Other) is higher in the NZP than APM series.

As discussed in several studies (e.g., O'Gorman & Schneider, 2009; Pendergrass & Hartmann, 2014; Seneviratne et al., 2021), the effect of global warming on atmospheric thermodynamic and dynamic processes could lead to changes in the distribution of daily P. Globally, P extremes are expected to increase at a rate similar to the rise in water vapor with warming (7.5%/K) or even higher because of dynamic circulation, whereas the mean P is predicted to increase at a smaller rate due to energy constraints. How these changes will occur at regional and local scales is still uncertain, and our investigation of the temporal changes in the number of GMs of NZP in the CONUS over the last four decades could provide useful insights. As shown in Fig. 5, we found overall low evidence of statistically significant trends, except for increases in the frequency of FRT in NE and TC in C. The low number of significant trends could be due to the small sample size of the count time series (as high as 39 years), combined with the presence of serial correlation that further reduces the test power (Farris et al., 2021; Serinaldi et al., 2018). Despite this, the spatial variability in the mean annual changes in GM frequency exhibits structured patterns with large regions with similar trend signs. These patterns are largely consistent with prior studies that analyzed the causes of observed trends in extreme P (but not of all P rates) in specific regions. In NE, Huang et al. (2018) found that the numbers of TC, FRT, and ETC increased in 1996-2016 relative to 1979-1995, as shown here, and that the higher number of TCs was the main cause of an abrupt rise in frequency and intensity of extreme P after 1996. The link between increasing frequency of TCs and more intense extreme P in NE was also documented by Henny et al. (2022). In a region including SE and part of C and NE, Skeeter et al. (2019) ascribed the intensification of extreme P to more frequent "moist tropical" days, which could be related to the increasing occurrence of TC presented here. Finally, while previous studies reported a rise in integrated water vapor of AR in the western regions (e.g., Gershunov et al., 2017), to our knowledge, the change in the annual frequency of this GM has not been explicitly studied.

646

616

617

618

619

620

621

622

623

624

625

626

627

628

629

630

631

632

633

634

635

636

637

638

639

640

641

642

643

644

b. Differences in statistical properties of precipitation distributions produced by the generating mechanisms

A major novel contribution of this paper is the investigation of whether the GMs lead to daily P accumulations with distinct statistical distributions for all NZP values and the subsamples of the APM that capture the extremes. This was done by focusing on the two most recurrent GMs that were shown to produce most of the P values across all sites. As shown in Fig. 6, FRT was found to be a dominant GM at all gauges in the CONUS, along with ETC in the large majority of the sites, AR in the western regions, and Other (NAM) in a few localized gauges close to the Gulf of Mexico coast (southern Arizona). Two-sample tests revealed the existence of welldefined regions (see Fig. 7 and Table 1) where the two dominant GMs generate NZP and APM series that likely belong to different statistical populations (labeled as Case 1), and of regions where the evidence of statistically different distributions is high only when considering all NZP values but not the subsamples of the APM (Case 2) and vice versa (Case 3). The physical interpretation of these findings will be the subject of future work and will involve the quantification of how the factors causing non-extreme and extreme P (e.g., water vapor availability and strength of vertical ascent) vary across the GMs, as suggested by Agel et al. (2015) who found different total P but similar extreme P magnitudes across the seasons in NE, like in our Case 2.

The inspection of the sample L-moments proved to be a very effective yet simple tool to explain the tests' results. To summarize and further explore the spatial variability of the differences between the P distributions, Fig. 12 shows maps of the ratio between the L-moments of the NZP and APM samples of (1) FRT, which is a dominant GM at all sites; and (2) the second dominant GM, which is either ETC, AR, NAM, or Others. Apart from some portions of the SW, S, and SE regions, the marginal distributions of P caused by FRT have lower means (ratio of  $\lambda_1 < 1$ ) but are more variable, positively skewed, and with heavier tails (ratios of  $\tau$ ,  $\tau_3$ , and  $\tau_4 > 1$ ) than the other mechanisms. The spatial patterns dramatically change when considering P extremes: if we exclude the W and NW regions dominated by AR, the APM samples of FRTs have a larger mean and lower variance throughout the country and, more significantly, in the S and SW regions. The ratios of  $\tau_3$  and  $\tau_4$  for the APM samples exhibit

instead random patterns, which are somewhat expected given the high uncertainty of these statistics with such short samples of extreme records. Finally, another effective way to explain the two-sample tests' results was the comparison of the GG and GEV distributions fitted to the NZP and APM series, respectively. These parametric distributions were found to capture quite well the two types of P series across GMs and geographic and climatic regions.

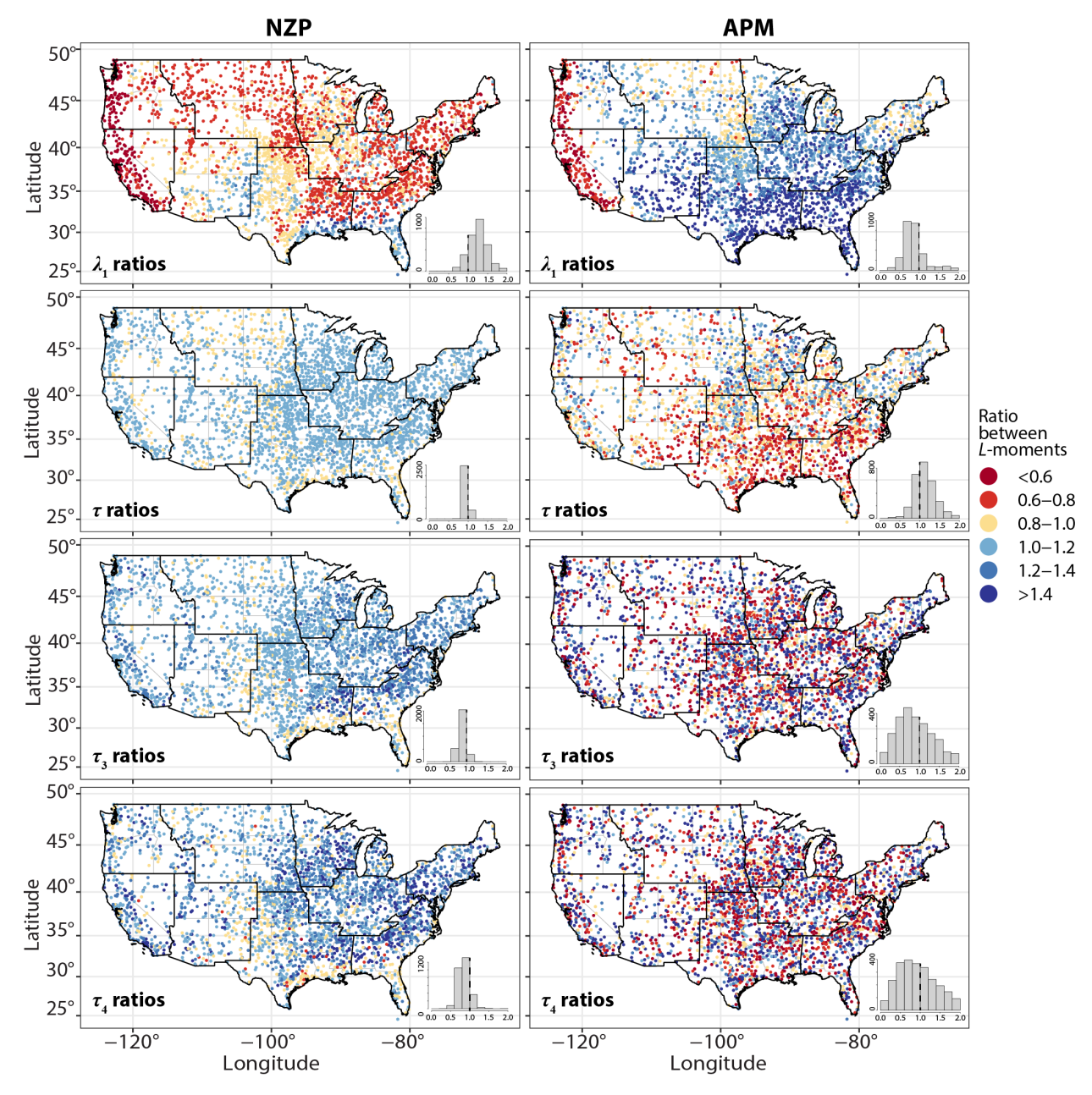


**Figure 12.** Ratio between the *L*-moment ratios ( $\lambda_1$ ,  $\tau$ ,  $\tau_3$ , and  $\tau_4$ ) of the NZP (left panels) and APM (right panels) samples associated with (1) FRT and (2) the second dominant mechanism (ETC, AR, Others, or NAM). The empirical histograms of the ratios are also reported to support the interpretation of the maps.

### 6. Conclusions

This study developed a CONUS-wide climatology of the occurrence of dominant GMs of daily P at 2861 gauges from 1980 to 2018. The GMs included TC, AR, ETC, FRT, and NAM, plus other unclassified mechanisms (Other). Unlike most of the prior work that focused only on extreme P, here the GMs associated with all nonzero P days were automatically extracted from the atmospheric reanalyses and existing datasets. The spatial variability of the annual and seasonal climatologies of the GMs associated with NZP and APM samples were presented and discussed, along with the analyses of trends in GM frequency. Next, the differences between the marginal and extreme distributions of P produced by the two most dominant GMs at each site were quantified using two-sample tests. *L*-moments and parametric distributions were used to explain and interpret the tests' results.

The results of this work have important implications for water resources managers and the design and management of infrastructure against extreme P, as they indicate locations and conditions where the use of mixed distributions (e.g., Mascaro, 2018; Miniussi et al., 2020) should be considered to improve the frequency analysis of all daily and extreme P. Moreover, these findings provide physical corroboration for the incorporation of nonstationarity in P frequency analysis. Results of this study could, in fact, be used as a benchmark to assess the GCMs' ability to reproduce the GMs of P in historical simulations; then, the frequencies of the GMs could be extracted from simulations under future climate scenarios of the most accurate GCMs and used in nonstationary statistical models of P frequency based on mixed distributions. Future work should be devoted to (1) expanding the GM classifications by including mesoscale convective systems (Fritsch et al., 1986) and ARs in other regions of the country (Slinskey et al., 2020); and (2) increasing the statistical significance of trend analyses in GM occurrence by quantifying the importance of internal climate variability vs. external forcings through climate simulations and atmospheric reanalysis, as done in recent promising studies (L. Dong & Leung, 2022; Huang et al., 2021; Kunkel, Karl, et al., 2020).

#### Acknowledgments

The authors thank three anonymous reviewers and the Editor whose comments helped to improve the quality of the manuscript. The authors also thank the support from the National Science Foundation (NSF) award #2221803 (PI Mascaro) and #2221808 (PI Kunkel):

- 718 "Collaborative Research: CAS Climate: Improving Nonstationary Intensity-Duration-
- 719 Frequency Analysis of Extreme Precipitation by Advancing Knowledge on the Generating
- 720 Mechanisms". M. A. also acknowledges support from Albaha University.
- 721 Data Availability Statement
- Precipitation data from the GHCNd rain gauge network are available at:
- 723 <a href="https://www.ncei.noaa.gov/products/land-based-station/global-historical-climatology-network-">https://www.ncei.noaa.gov/products/land-based-station/global-historical-climatology-network-</a>
- daily. The generating mechanisms for the station precipitation data are at
- 725 <u>https://zenodo.org/doi/10.5281/zenodo.10724690</u>

728

729

730

731

732

733

734

735

727 APPENDIX

### **Appendix A: Count time series models**

A count time series process can be generally defined as  $Y = \{Y_t; t \in \mathbb{N}^+\}$ . We generated stationary synthetic count time series that adequately reproduce marginal distribution and serial correlation of the observed sample count data,  $\{y_t\}$ , to compute the null distribution of the trend test statistic as described in Section 3b. To introduce the count time series models, we first describe the Poisson (Poi) and negative binomial (NB) discrete probability distributions which were found to capture well the marginal distributions of the samples  $\{y_t\}$ . The probability mass function (pmf) of the Poi distribution is:

736 
$$P_{Poi}(Y = y; \mu) = \frac{e^{-\mu}\mu^{y}}{y!} \qquad y = 0, 1, 2, ...$$
(A1)

737 with parameter  $\mu > 0$ , and equal mean and variance. The pmf of the NB distribution is:

738 
$$P_{NB}\left(Y=y;\theta,\frac{p}{1+p}\right) = \binom{\theta+y-1}{y} \frac{p^{y}}{(1+p)^{\theta+y}} \qquad y=0,1,2,\dots,$$
 (A2)

- 739 with two parameters  $\theta > 0$  and p > 0 that allow representing overdispersed count data with
- variance larger than the mean (Colin & Pravin, 1998). Note that  $\left(\frac{p}{1+p}\right)$  is the probability of
- failure that appears in the alternative form of the NB distribution that is often utilized (see, e.g.,
- 742 D. S. Wilks, 2019).
- For each observed sample  $\{y_t\}$ , we considered two count time series models that could reproduce its serial correlation structure, but with Poi and NB marginals, respectively; we then

- selected the best-performing model based on the lowest Akaike Information Criteria. To do this,
- we first computed the lag-1 serial correlation,  $\rho_1$ , and considered the series to exhibit serial
- correlation if  $\rho_1 > 0$ , and to be uncorrelated if  $\rho_1 \le 0$ . For the latter case, the two count time series
- models consisted of simply simulating random variates of either the Poi or NB distribution with
- parameters estimated through maximum likelihood. For serially correlated series with Poi
- marginal distribution, we adopted the Poisson integer autoregressive model of order 1 or
- PoiINAR(1) (Al-Osh & Alzaid, 1987; Brännäs, 1995). A stationary process  $\{Y_t\}$  is defined
- 752 PoiINAR(1) with parameters  $\{\mu_Y, \beta\}$  if:

$$Y_t = \beta \circ Y_{t-1} + \epsilon_t, \tag{A3}$$

- where  $\{\epsilon_t\}$  is an independent and identically distributed (i.i.d.) integer Poisson random variable
- with parameter  $\mu_{\varepsilon}$ , and "o" is the binomial thinning operator defined as:

756 
$$\beta \circ Y = \sum_{i=1}^{Y} B_i, \qquad Y > 0, \tag{A4}$$

- 757 where  $\{B_i\}$  are i.i.d. variates of a Bernoulli distribution with parameter  $\beta$  and pmf
- 758  $P_{Bern}(B=b;\beta) = \beta^b (1-\beta)^{1-b}, b \in \{0,1\}$ . The variable  $\{Y_t\}$  is also Poisson-distributed with
- 759 parameter  $\mu_Y = \mu_{\epsilon}/(1-\beta)$ .
- Serially correlated time series with NB marginal distribution were simulated with the
- negative binomial INAR(1) model or NBINAR(1) (Ristic et al., 2012). A stationary process  $\{Y_t\}$
- 762 is defined NBINAR(1) with parameters  $\{p, \theta, \alpha\}$  if:

$$Y_t = \alpha * Y_{t-1} + \epsilon_t, \tag{A5}$$

- where  $\{\epsilon_t\}$  is an i.i.d. integer random variable with the distribution provided by Ristić et al.
- 765 (2012; their equation (2)) with parameters  $\theta > 0$ , p > 0, and  $\alpha \in [0, p/(1+p)]$ . The operator "\*"
- is the negative Binomial thinning operator:

767 
$$\alpha * Y = \sum_{i=1}^{Y} G_i, \quad Y > 0,$$
 (A6)

- 768 where  $\{G_i\}$  are i.i.d. variates of a geometric distribution with parameter  $\left(\frac{\alpha}{1+\alpha}\right)$  and pmf
- 769  $P_{geo}\left(G=g;\frac{\alpha}{1+\alpha}\right)=\frac{\alpha^g}{(1+\alpha)^{g+1}}, g=0, 1, 2, \dots$  Note that  $\left(\frac{\alpha}{1+\alpha}\right)$  is the probability of failure that
- appears in the other popular parameterization of the geometric distribution. The variable  $\{Y_t\}$  is
- NB-distributed with parameters  $\theta$  and  $\left(\frac{p}{1+p}\right)$ . For both the PoiINAR(1) and NBINAR(1) models,
- parameters were estimated through conditional least squares (CLS) following Ristíc et al. (2012).

However, because of the relatively small sample size, it was found that the CLS estimates of  $\beta$  and  $\alpha$  led to an underestimation of the observed  $\rho_1$ , especially for smaller values. Monte Carlo simulations were then conducted with the two models to find empirical relationships that were used to bias correct the CLS estimates of  $\beta$  and  $\alpha$  as a function of the observed  $\rho_1$ .

### **Appendix B: Two-sample statistical tests**

The Wilcoxon test is a non-parametric test whose null hypothesis  $H_0$  is that both samples have equal median. The test statistic is  $U = R_1 - \frac{n_1}{2}(n_1 + 1)$ , where  $R_1$  is the sum of the ranks of one of the samples with size  $n_1$ . The null distribution of U is Gaussian for sample sizes larger than 10. The Kolmogorov–Smirnov test is also non-parametric, and its  $H_0$  is that the samples are drawn from the same distribution. The statistic is  $D_s = \max_x |F_1(x) - F_2(x)|$ , where  $F_1(x)$  and  $F_2(x)$  are the empirical cumulative distribution functions of the first and second samples, respectively. The p-value is computed through the Kolmogorov distribution or other approximations. The likelihood ratio test has the same  $H_0$  as the Kolmogorov–Smirnov test and requires assuming parametric forms for the distribution of samples 1 and 2 and of the two samples combined. Let us defined  $G_1(x; \hat{\theta}_1)$ ,  $G_2(x; \hat{\theta}_2)$ , and  $G_0(x; \hat{\theta}_0)$  as such distributions with parameters  $\widehat{\theta}_1$ ,  $\widehat{\theta}_2$ , and  $\widehat{\theta}_0$  estimated on the corresponding samples  $x_1$ ,  $x_2$ , and  $x_0 = \{x_1, x_2\}$ . The test statistic is  $\Lambda^* = 2[L_1(\widehat{\theta}_1; x_1) + L_2(\widehat{\theta}_2; x_2) - L_0(\widehat{\theta}_0; x_0)]$ , where  $L_k(\widehat{\boldsymbol{\theta}}_k; \boldsymbol{x}_k)$  is the log-likelihood of the corresponding distribution  $G_k(x; \widehat{\boldsymbol{\theta}}_k)$ , with k = 0, 1, and 2. The null distribution is the  $\chi^2$  with degrees of freedom  $\nu = m_1 + m_2 - m_0$ , where  $m_k$  is the number of parameters of the k-th distribution. Here, we used the generalized gamma (GG) and the generalized extreme value (GEV) as parametric distributions for the NZP and APM series (see Appendix C).

### Appendix C: The generalized gamma and generalized extreme value distributions

The cumulative distribution function (CDF) of the generalized gamma (GG) distribution

797 is:

777

778

779

780

781

782

783

784

785

786

787

788

789

790

791

792

793

794

795

798 
$$F_{GG}(x) = 1 - \Gamma\left(\frac{\gamma_1}{\gamma_2}, \left(\frac{x}{\beta}\right)^{\gamma_2}\right) / \Gamma\left(\frac{\gamma_1}{\gamma_2}\right), \tag{C1}$$

- 799 which is defined for  $x \ge 0$  and where  $\gamma_1 > 0$  and  $\gamma_2 > 0$  are two shape parameters,  $\beta > 0$  is the
- scale parameter, and  $\Gamma(\cdot,\cdot)$  and  $\Gamma(\cdot)$  are the incomplete and complete gamma functions,
- respectively. The CDF of the generalized extreme value (GEV) distribution is:

802 
$$F_{GEV}(x;\xi,\mu,\sigma) = \begin{cases} \exp\left\{-\left(1 + \xi \frac{x-\mu}{\sigma}\right)^{-\frac{1}{\xi}}\right\} & \xi \neq 0\\ \exp\left\{-\exp\left(-\frac{x-\mu}{\sigma}\right)\right\} & \xi = 0 \end{cases}$$
(C2)

- 803 where  $\xi \in (-\infty, +\infty)$  is the shape parameter,  $\mu \in (-\infty, +\infty)$  the location parameter, and  $\sigma > 0$  the
- scale parameter. The GEV is defined in the sets  $-\infty < x < \infty$  if  $\xi = 0$ ,  $\mu \frac{\sigma}{\xi} \le x < \infty$  if  $\xi > 0$ ,
- 805 and  $-\infty < x \le \mu \frac{\sigma}{\xi}$  if  $\xi < 0$ .

806 REFERENCES

- Adams, D. K., & Comrie, A. C. (1997). The North American Monsoon. Bulletin of the American
- 808 *Meteorological Society*, 78(10), 2197–2213. https://doi.org/10.1175/1520-0477(1997)078
- Agel, L., Barlow, M., Qian, J. H., Colby, F., Douglas, E., & Eichler, T. (2015). Climatology of
- daily precipitation and extreme precipitation events in the Northeast United States. *Journal*
- 811 of Hydrometeorology, 16(6), 2537–2557. https://doi.org/10.1175/JHM-D-14-0147.1
- 812 Al-Osh, M. A., & Alzaid, A. A. (1987). FIRST-ORDER INTEGER-VALUED
- 813 AUTOREGRESSIVE (INAR(1)) PROCESS. Journal of Time Series Analysis, 8(3), 261–
- 814 275. https://doi.org/10.1111/J.1467-9892.1987.TB00438.X
- Barlow, M., Gutowski, W. J., Gyakum, J. R., Katz, R. W., Lim, Y. K., Schumacher, R. S.,
- Wehner, M. F., Agel, L., Bosilovich, M., Collow, A., Gershunov, A., Grotjahn, R., Leung,
- 817 R., Milrad, S., & Min, S. K. (2019). North American extreme precipitation events and
- related large-scale meteorological patterns: a review of statistical methods, dynamics,
- modeling, and trends. Climate Dynamics, 53(11), 6835–6875.
- 820 https://doi.org/10.1007/S00382-019-04958-Z/FIGURES/2
- 821 Biard, J. C., & Kunkel, K. E. (2019). Automated detection of weather fronts using a deep
- learning neural network. Advances in Statistical Climatology, Meteorology and
- 823 Oceanography, 5(2), 147–160. https://doi.org/10.5194/ASCMO-5-147-2019

- Blanchet, J., Ceresetti, D., Molinié, G., & Creutin, J. D. (2016). A regional GEV scale-invariant
- framework for Intensity-Duration-Frequency analysis. *Journal of Hydrology*, 540, 82–95.
- 826 https://doi.org/10.1016/J.JHYDROL.2016.06.007
- 827 Bonnin, G. M., Martin, D., Lin, B., Parzybok, T., Yekta, M., & Riley, D. (2004). Precipitation-
- Frequency Atlas of the United States. NOAA Atlas 14: Precipitation-Frequency Atlas of the
- 829 *United States.*
- 830 Brännäs, K. (1995). EXPLANATORY VARIABLES IN THE AR(1) COUNT.
- Cann, K. F., Thomas, D. R., Salmon, R. L., Wyn-Jones, A. P., & Kay, D. (2013). Extreme water-
- related weather events and waterborne disease. *Epidemiology & Infection*, 141(4), 671–686.
- https://doi.org/10.1017/S0950268812001653
- 834 Catto, J. L., & Pfahl, S. (2013). The importance of fronts for extreme precipitation. *Journal of*
- 835 *Geophysical Research: Atmospheres*, 118(19), 10,791-10,801.
- https://doi.org/10.1002/JGRD.50852
- 837 Colin, C. A., & Pravin, T. (1988). Regression analysis of count data, Second edition. Regression
- 838 Analysis of Count Data, Second Edition, 1–567.
- https://doi.org/10.1017/CBO9781139013567
- Davenport, F. V., & Diffenbaugh, N. S. (2021). Using Machine Learning to Analyze Physical
- Causes of Climate Change: A Case Study of U.S. Midwest Extreme Precipitation.
- *Geophysical Research Letters*, 48(15), e2021GL093787.
- https://doi.org/10.1029/2021GL093787
- Deidda, R., Hellies, M., & Langousis, A. (2021). A critical analysis of the shortcomings in
- spatial frequency analysis of rainfall extremes based on homogeneous regions and a
- comparison with a hierarchical boundaryless approach. Stochastic Environmental Research
- 847 and Risk Assessment, 35(12), 2605–2628. https://doi.org/10.1007/S00477-021-02008-X
- 848 Dong, L., & Leung, L. R. (2022). Roles of External Forcing and Internal Variability in
- Precipitation Changes of a Sub-Region of the U.S. Mid-Atlantic During 1979–2019.
- *Journal of Geophysical Research: Atmospheres*, 127(22), e2022JD037493.
- https://doi.org/10.1029/2022JD037493
- 852 Dong, Q., Wang, W., Kunkel, K. E., Shao, Q., Xing, W., & Wei, J. (2021). Heterogeneous
- response of global precipitation concentration to global warming. *International Journal of*
- 854 *Climatology*, 41(S1), E2347–E2359. https://doi.org/10.1002/JOC.6851

- Eekhout, J. P. C., Hunink, J. E., Terink, W., & De Vente, J. (2018). Why increased extreme
- precipitation under climate change negatively affects water security. Hydrology and Earth
- 857 System Sciences, 22(11), 5935–5946. https://doi.org/10.5194/HESS-22-5935-2018
- 858 Emori, S., & Brown, S. J. (2005). Dynamic and thermodynamic changes in mean and extreme
- precipitation under changed climate. *Geophysical Research Letters*, 32(17), 1–5.
- https://doi.org/10.1029/2005GL023272
- 861 Eyring, V., N.P. Gillett, K.M. Achuta Rao, R. Barimalala, M. Barreiro Parrillo, N. Bellouin, C.
- Cassou, P.J. Durack, Y. Kosaka, S. McGregor, S. Min, O. Morgenstern, and Y. Sun (2021):
- Human Influence on the Climate System. In Climate Change 2021: The Physical Science
- Basis. Contribution of Working Group I to the Sixth Assessment Report of the
- Intergovernmental Panel on Climate Change [Masson-Delmotte, V., P. Zhai, A. Pirani, S.L.
- Connors, C. Péan, S. Berger, N. Caud, Y. Chen, L. Goldfarb, M.I. Gomis, M. Huang, K.
- Leitzell, E. Lonnoy, J.B.R. Matthews, T.K. Maycock, T. Waterfield, O. Yelekçi, R. Yu, and
- B. Zhou (eds.)]. Cambridge University Press, Cambridge, United Kingdom and New York,
- NY, USA, pp. 423–552, doi:10.1017/9781009157896.005.
- 870 Farris, S., Deidda, R., Viola, F., & Mascaro, G. (2021). On the Role of Serial Correlation and
- Field Significance in Detecting Changes in Extreme Precipitation Frequency. *Water*
- 872 Resources Research, 57(11), e2021WR030172. https://doi.org/10.1029/2021WR030172
- Fritsch, J. M., Kane, R. J., & Chelius, C. R. (1986). The Contribution of Mesoscale Convective
- Weather Systems to the Warm-Season Precipitation in the United States. *Source: Journal of*
- 875 Climate and Applied Meteorology, 25(10), 1333–1345. https://about.jstor.org/terms
- 676 Gelaro, R., McCarty, W., Suárez, M. J., Todling, R., Molod, A., Takacs, L., Randles, C. A.,
- Darmenov, A., Bosilovich, M. G., Reichle, R., Wargan, K., Coy, L., Cullather, R., Draper,
- 878 C., Akella, S., Buchard, V., Conaty, A., da Silva, A. M., Gu, W., ... Zhao, B. (2017). The
- Modern-Era Retrospective Analysis for Research and Applications, Version 2 (MERRA-2).
- Journal of Climate, Volume 30(Iss 13), 5419. https://doi.org/10.1175/JCLI-D-16-0758.1
- Gershunov, A., Benmarhnia, T., & Aguilera, R. (2018). Human health implications of extreme
- precipitation events and water quality in California, USA: a canonical correlation analysis.
- 883 The Lancet Planetary Health, 2, S9. https://doi.org/10.1016/S2542-5196(18)30094-9

- Gershunov, A., Shulgina, T., Ralph, F. M., Lavers, D. A., & Rutz, J. J. (2017). Assessing the
- climate-scale variability of atmospheric rivers affecting western North America.
- 886 Geophysical Research Letters, 44(15), 7900–7908. https://doi.org/10.1002/2017GL074175
- Guan, X., Mascaro, G., Sampson, D., & Maciejewski, R. (2020). A metropolitan scale water
- management analysis of the food-energy-water nexus. Science of The Total Environment,
- 701, 134478. https://doi.org/10.1016/J.SCITOTENV.2019.134478
- Henny, L., Thorncroft, C. D., & Bosart, L. F. (2022). Changes in Large-Scale Fall Extreme
- Precipitation in the Mid-Atlantic and Northeast United States, 1979–2019. *Journal of*
- 892 *Climate*, 35(20), 3047–3070. https://doi.org/10.1175/JCLI-D-21-0953.1
- Henny, L., Thorncroft, C. D., & Bosart, L. F. (2023). Changes in Seasonal Large-Scale Extreme
- Precipitation in the Mid-Atlantic and Northeast United States, 1979–2019. *Journal of*
- 895 *Climate*, *36*(4), 1017–1042. <a href="https://doi.org/10.1175/JCLI-D-22-0088.1">https://doi.org/10.1175/JCLI-D-22-0088.1</a>
- Holton, J.R. (1992). An Introduction to Dynamic Meteorology, Third Edition. Academic Press.
- Hosking, J. R. M. (1990). L-Moments: Analysis and Estimation of Distributions Using Linear
- 898 Combinations of Order Statistics. Source: Journal of the Royal Statistical Society. Series B
- 899 *(Methodological)*, *52*(1), 105–124.
- Hosking, J. R. M., & Wallis, J. R. (1997). Regional Frequency Analysis. In *Regional Frequency*
- 901 Analysis. Cambridge University Press. https://doi.org/10.1017/cbo9780511529443
- Hou, A. Y., Kakar, R. K., Neeck, S., Azarbarzin, A. A., Kummerow, C. D., Kojima, M., Oki, R.,
- Nakamura, K., & Iguchi, T. (2014). The Global Precipitation Measurement Mission.
- 904 Bulletin of the American Meteorological Society, 95(5), 701–722.
- 905 https://doi.org/10.1175/BAMS-D-13-00164.1
- Huang, H., Patricola, C. M., Winter, J. M., Osterberg, E. C., & Mankin, J. S. (2021). Rise in
- Northeast US extreme precipitation caused by Atlantic variability and climate change.
- 908 https://doi.org/10.1016/j.wace.2021.100351
- Huang, H., Winter, J. M., & Osterberg, E. C. (2018). Mechanisms of Abrupt Extreme
- Precipitation Change Over the Northeastern United States. *Journal of Geophysical*
- 911 Research: Atmospheres, 123(14), 7179–7192. https://doi.org/10.1029/2017JD028136
- Janssen, E., Wuebbles, D. J., Kunkel, K. E., Olsen, S. C., & Goodman, A. (2014). Observational-
- and model-based trends and projections of extreme precipitation over the contiguous United
- 914 States. *Earth's Future*, 2(2), 99–113. https://doi.org/10.1002/2013EF000185

- 815 Kalnay, E.M., 1996. coauthors, The NCEP/NCAR Reanalysis project. Bulletin of the American
- 916 *Meteorological Society*, 77, 437-471.
- 917 Karl, T., & Koss, W. J. 1931-. (1984). Regional and national monthly, seasonal, and annual
- 918 temperature weighted by area, 1895-1983.
- 919 https://repository.library.noaa.gov/view/noaa/10238
- 920 Knapp, K. R., Kruk, M. C., Levinson, D. H., Diamond, H. J., & Neumann, C. J. (2010). The
- 921 International Best Track Archive for Climate Stewardship (IBTrACS): Unifying Tropical
- 922 Cyclone Data. Bulletin of the American Meteorological Society, 91(3), 363–376.
- 923 https://doi.org/10.1175/2009BAMS2755.1
- 824 Kolmogorov-Smirnov, A., Kolmogorov, A., & Kolmogorov, M. (1933). Sulla determinazione
- 925 empírica di uma legge di distribuzione.
- Wunkel, K. E., Easterling, D. R., Kristovich, D. A. R., Gleason, B., Stoecker, L., & Smith, R.
- 927 (2012). Meteorological Causes of the Secular Variations in Observed Extreme Precipitation
- 928 Events for the Conterminous United States. *Journal of Hydrometeorology*, 13(3), 1131–
- 929 1141. https://doi.org/10.1175/JHM-D-11-0108.1
- 930 Kunkel, K. E., Karl, T. R., Squires, M. F., Yin, X., Stegall, S. T., & Easterling, D. R. (2020).
- Precipitation Extremes: Trends and Relationships with Average Precipitation and
- Precipitable Water in the Contiguous United States. *Journal of Applied Meteorology and*
- 933 *Climatology*, *59*(1), 125–142. https://doi.org/10.1175/JAMC-D-19-0185.1
- Wunkel, K. E., Stevens, S. E., Stevens, L. E., & Karl, T. R. (2020). Observed Climatological
- Relationships of Extreme Daily Precipitation Events With Precipitable Water and Vertical
- Velocity in the Contiguous United States. *Geophysical Research Letters*, 47(12).
- 937 https://doi.org/10.1029/2019GL086721
- Lee, J.-Y., J. Marotzke, G. Bala, L. Cao, S. Corti, J.P. Dunne, F. Engelbrecht, E. Fischer, J.C.
- Fyfe, C. Jones, A. Maycock, J. Mutemi, O. Ndiaye, S. Panickal, and T. Zhou (2021): Future
- Global Climate: Scenario-Based Projections and Near Term Information. In *Climate*
- Change 2021: The Physical Science Basis. Contribution of Working Group I to the Sixth
- 942 Assessment Report of the Intergovernmental Panel on Climate Change [Masson-Delmotte,
- 943 V., P. Zhai, A. Pirani, S.L. Connors, C. Péan, S. Berger, N. Caud, Y. Chen, L. Goldfarb,
- 944 M.I. Gomis, M. Huang, K. Leitzell, E. Lonnoy, J.B.R. Matthews, T.K. Maycock, T.
- 945 Waterfield, O. Yelekçi, R. Yu, and B. Zhou (eds.)]. Cambridge University Press,

946 Cambridge, United Kingdom and New York, NY, USA, pp. 553–672, 947 doi:10.1017/9781009157896.006 948 Lopez-Cantu, T., Prein, A. F., & Samaras, C. (2020). Uncertainties in Future U.S. Extreme 949 Precipitation From Downscaled Climate Projections. Geophysical Research Letters, 47(9), 950 e2019GL086797. https://doi.org/10.1029/2019GL086797 951 Marquardt Collow, A. B., Bosilovich, M. G., & Koster, R. D. (2016). Large-Scale Influences on 952 Summertime Extreme Precipitation in the Northeastern United States. *Journal of* 953 Hydrometeorology, 17(12), 3045–3061. https://doi.org/10.1175/JHM-D-16-0091.1 954 Mascaro, G. (2018). On the distributions of annual and seasonal daily rainfall extremes in central 955 Arizona and their spatial variability. *Journal of Hydrology*, 559, 266–281. 956 https://doi.org/10.1016/J.JHYDROL.2018.02.011 957 Mascaro, G. (2020). Comparison of Local, Regional, and Scaling Models for Rainfall Intensity-958 Duration-Frequency Analysis. Journal of Applied Meteorology and Climatology, 59(9), 959 1519–1536. https://doi.org/10.1175/JAMC-D-20-0094.1Mascaro, G. (2024). On the power 960 of popular two-sample tests applied to precipitation and discharge series. Stochastic 961 Environmental Research and Risk Assessment. https://doi.org/10.1007/S00477-024-02709-962 Z 963 Mascaro, G., Papalexiou, S. M., & Wright, D. B. (2023). Advancing Characterization and 964 Modeling of Space-Time Correlation Structure and Marginal Distribution of Short-Duration 965 Precipitation. Advances in Water Resources, 177. 966 https://doi.org/10.1016/J.ADVWATRES.2023.104451 967 Miniussi, A., Villarini, G., & Marani, M. (2020). Analyses Through the Metastatistical Extreme 968 Value Distribution Identify Contributions of Tropical Cyclones to Rainfall Extremes in the 969 Eastern United States. Geophysical Research Letters, 47(7), e2020GL087238. 970 https://doi.org/10.1029/2020GL087238 971 Moore, B. J., Mahoney, K. M., Sukovich, E. M., Cifelli, R., & Hamill, T. M. (2015). 972 Climatology and Environmental Characteristics of Extreme Precipitation Events in the 973 Southeastern United States. Monthly Weather Review, 143(3), 718–741. 974 https://doi.org/10.1175/MWR-D-14-00065.1

- 975 Mullens, E. D. (2021). Meteorological cause and characteristics of widespread heavy
- precipitation in the Texas Gulf watershed 2003–2018. *International Journal of Climatology*,
- 977 41(6), 3743–3760. https://doi.org/10.1002/JOC.7046
- 978 NCEI. (n.d.). Retrieved August 31, 2023, from <a href="https://www.ncei.noaa.gov/products/land-based-">https://www.ncei.noaa.gov/products/land-based-</a>
- 979 station/global-historical-climatology-network-daily
- 980 O'Gorman, P. A., & Schneider, T. (2009). The physical basis for increases in precipitation
- extremes in simulations of 21st-century climate change. *Proceedings of the National*
- Academy of Sciences of the United States of America, 106(35), 14773–14777.
- 983 https://doi.org/10.1073/PNAS.0907610106/SUPPL\_FILE/0907610106SI.PDF
- Papalexiou, S. M., & Koutsoyiannis, D. (2012). Entropy based derivation of probability
- distributions: A case study to daily rainfall. *Advances in Water Resources*, 45, 51–57.
- 986 https://doi.org/10.1016/J.ADVWATRES.2011.11.007
- Papalexiou, S. M., & Koutsoyiannis, D. (2013). Battle of extreme value distributions: A global
- 988 survey on extreme daily rainfall. *Water Resources Research*, 49(1), 187–201.
- 989 https://doi.org/10.1029/2012WR012557
- 990 Papalexiou, S. M. (2022). Rainfall Generation Revisited: Introducing CoSMoS-2s and
- Advancing Copula-Based Intermittent Time Series Modeling. Water Resources Research,
- 992 58(6), e2021WR031641. https://doi.org/10.1029/2021WR031641
- 993 Pendergrass, A. G., & Hartmann, D. L. (2014). Changes in the Distribution of Rain Frequency
- and Intensity in Response to Global Warming. *Journal of Climate*, 27(22), 8372–8383.
- 995 https://doi.org/10.1175/JCLI-D-14-00183.1
- Prein, A. F., Liu, C., Ikeda, K., Trier, S. B., Rasmussen, R. M., Holland, G. J., & Clark, M. P.
- 997 (2017). Increased rainfall volume from future convective storms in the US. *Nature Climate*
- 998 Change 2017 7:12, 7(12), 880–884. https://doi.org/10.1038/s41558-017-0007-7
- 999 Prein, A. F., & Mearns, L. O. (2021). U.S. Extreme Precipitation Weather Types Increased in
- Frequency During the 20th Century. *Journal of Geophysical Research: Atmospheres*,
- 1001 126(7), e2020JD034287. https://doi.org/10.1029/2020JD034287
- 1002 Priestley, M. D. K., Ackerley, D., Catto, J. L., Hodges, K. I., McDonald, R. E., & Lee, R. W.
- 1003 (2020). An Overview of the Extratropical Storm Tracks in CMIP6 Historical Simulations.
- Journal of Climate, 33(15), 6315–6343. https://doi.org/10.1175/JCLI-D-19-0928.1

- Ristíc, M. M., Nastíc, A. S., & Bakouch, H. S. (2012). Estimation in an Integer-Valued
- Autoregressive Process with Negative Binomial Marginals (NBINAR(1)). *Communications*
- in Statistics Theory and Methods, 41(4), 606–618.
- 1008 https://doi.org/10.1080/03610926.2010.529528
- Schumacher, R. S., & Rasmussen, K. L. (2020). The formation, character and changing nature of
- mesoscale convective systems. *Nature Reviews Earth and Environment*, 1(6), 300–314.
- 1011 https://doi.org/10.1038/S43017-020-0057-7
- Seneviratne, S.I., X. Zhang, M. Adnan, W. Badi, C. Dereczynski, A. Di Luca, S. Ghosh, I.
- 1013 Iskandar, J. Kossin, S. Lewis, F. Otto, I. Pinto, M. Satoh, S.M. Vicente-Serrano, M.
- Wehner, and B. Zhou, 2021: Weather and Climate Extreme Events in a Changing Climate.
- In Climate Change 2021: The Physical Science Basis. Contribution of Working Group I to
- the Sixth Assessment Report of the Intergovernmental Panel on Climate Change [Masson-
- Delmotte, V., P. Zhai, A. Pirani, S.L. Connors, C. Péan, S. Berger, N. Caud, Y. Chen, L.
- Goldfarb, M.I. Gomis, M. Huang, K. Leitzell, E. Lonnoy, J.B.R. Matthews, T.K. Maycock,
- T. Waterfield, O. Yelekçi, R. Yu, and B. Zhou (eds.)]. Cambridge University Press,
- 1020 Cambridge, United Kingdom and New York, NY, USA, pp. 1513–1766,
- 1021 doi: 10.1017/9781009157896.013.
- 1022 Serinaldi, F., Kilsby, C. G., & Lombardo, F. (2018). Untenable nonstationarity: An assessment
- of the fitness for purpose of trend tests in hydrology. Advances in Water Resources, 111,
- 1024 132–155. https://doi.org/10.1016/J.ADVWATRES.2017.10.015
- Sheridan, S. C. (2002). The redevelopment of a weather-type classification scheme for North
- 1026 America. *International Journal of Climatology*, 22(1), 51–68.
- 1027 https://doi.org/10.1002/JOC.709
- Skeeter, W. J., Senkbeil, J. C., & Keellings, D. J. (2019). Spatial and temporal changes in the
- frequency and magnitude of intense precipitation events in the southeastern United States.
- International Journal of Climatology, 39(2), 768–782. https://doi.org/10.1002/JOC.5841
- 1031 Slinskey, E. A., Loikith, P. C., Waliser, D. E., Guan, B., & Martin, A. (2020). A climatology of
- atmospheric rivers and associated precipitation for the seven U.S. national climate
- assessment regions. *Journal of Hydrometeorology*, 21(11), 2439–2456.
- 1034 https://doi.org/10.1175/JHM-D-20-0039.1

- 1035 Trenberth, K. E. (1999). Conceptual framework for changes of extremes of the hydrological
- 1036 cycle with climate change. *Climatic Change*, 42(1), 327–339.
- 1037 https://doi.org/10.1023/A:1005488920935/METRICS
- 1038 Underwood, B. S., Mascaro, G., Chester, M. V., Fraser, A., Lopez-Cantu, T., & Samaras, C.
- 1039 (2020). Past and Present Design Practices and Uncertainty in Climate Projections are
- 1040 Challenges for Designing Infrastructure to Future Conditions. *Journal of Infrastructure*
- 1041 Systems, 26(3). https://doi.org/10.1061/(ASCE)IS.1943-555X.0000567
- Wang, X. L., Feng, Y., Compo, G. P., Swail, V. R., Zwiers, F. W., Allan, R. J., & Sardeshmukh,
- P. D. (2013). Trends and low frequency variability of extra-tropical cyclone activity in the
- ensemble of twentieth century reanalysis. *Climate Dynamics*, 40(11–12), 2775–2800.
- 1045 https://doi.org/10.1007/S00382-012-1450-9/METRICS
- Wilcox, K. R., Shi, Z., Gherardi, L. A., Lemoine, N. P., Koerner, S. E., Hoover, D. L., Bork, E.,
- Byrne, K. M., Cahill, J., Collins, S. L., Evans, S., Gilgen, A. K., Holub, P., Jiang, L.,
- Knapp, A. K., LeCain, D., Liang, J., Garcia-Palacios, P., Peñuelas, J., ... Luo, Y. (2017).
- 1049 Asymmetric responses of primary productivity to precipitation extremes: A synthesis of
- grassland precipitation manipulation experiments. Global Change Biology, 23(10), 4376–
- 1051 4385. https://doi.org/10.1111/GCB.13706
- Wilcoxon, F. (1945). Individual Comparisons by Ranking Methods. *Bulletin*, 1(6), 80–83.
- Wilks, D. S. (2006). On "Field Significance" and the False Discovery Rate. *Journal of Applied*
- 1054 *Meteorology and Climatology*, 45(9), 1181–1189. https://doi.org/10.1175/JAM2404.1
- Wilks, D. S. (2019). Statistical Methods in the Atmospheric Sciences, Fourth Edition. Statistical
- 1056 *Methods in the Atmospheric Sciences, Fourth Edition*, 1–818.
- 1057 https://doi.org/10.1016/C2017-0-03921-6
- Wilks, S. S. (1938). The Large-Sample Distribution of the Likelihood Ratio for Testing
- 1059 Composite Hypotheses. *Https://Doi.Org/10.1214/Aoms/1177732360*, *9*(1), 60–62.
- 1060 https://doi.org/10.1214/AOMS/1177732360
- Zaghloul, M., Papalexiou, S. M., Elshorbagy, A., & Coulibaly, P. (2020). Revisiting flood peak
- distributions: A pan-Canadian investigation. *Advances in Water Resources*, 145, 103720.
- 1063 https://doi.org/10.1016/J.ADVWATRES.2020.103720

1064	Zhang, W., & Villarini, G. (2021). Greenhouse gases drove the increasing trends in spring
1065	precipitation across the central USA. Philosophical Transactions. Series A, Mathematical,
1066	Physical, and Engineering Sciences, 379(2195). https://doi.org/10.1098/RSTA.2019.0553
1067	Zhao, S., Deng, Y., & Black, R. X. (2017). A Dynamical and Statistical Characterization of U.S.
1068	Extreme Precipitation Events and Their Associated Large-Scale Meteorological Patterns.
1069	Journal of Climate, 30(4), 1307–1326. https://doi.org/10.1175/JCLI-D-15-0910.1
1070	